ELSEVIER

Structure of hydrated Zn^{2+} at the rutile TiO_2 (110)-aqueous solution interface: Comparison of X-ray standing wave, X-ray absorption spectroscopy, and density functional theory results ☆

Zhan Zhang [a,*], Paul Fenter [a], Shelly D. Kelly [a], Jeffery G. Catalano [a], Andrei V. Bandura [b],
James D. Kubicki [c], Jorge O. Sofo [c], David J. Wesolowski [d], Michael L. Machesky [e],
Neil C. Sturchio [f], Michael J. Bedzyk [g]

[a] *Argonne National Laboratory, Argonne, IL, USA*
[b] *St. Petersburg State University, St. Petersburg, Russia*
[c] *Pennsylvania State University, University Park, PA, USA*
[d] *Oak Ridge National Laboratory, Oak Ridge, TN, USA*
[e] *Illinois State Water Survey, Champaign, IL, USA*
[f] *University of Illinois at Chicago, Chicago, IL, USA*
[g] *Northwestern University, Evanston, IL, USA*

Abstract

Adsorption of Zn^{2+} at the rutile TiO_2 (110)-aqueous interface was studied with Bragg-reflection X-ray standing waves (XSW), polarization-dependent surface extended X-ray absorption fine structure (EXAFS) spectroscopy, and density functional theory (DFT) calculations to understand the interrelated issues of adsorption site, its occupancy, ion–oxygen coordination and hydrolysis. At pH 8, Zn^{2+} was found to adsorb as an inner-sphere complex at two different sites, i.e., monodentate above the bridging O site and bidentate between two neighboring terminal O sites. EXAFS results directly revealed a four or fivefold first shell coordination environment for adsorbed Zn^{2+} instead of the sixfold coordination found for aqueous species at this pH. DFT calculations confirmed the energetic stability of a lower coordination environment for the adsorbed species and revealed that the change to this coordination environment is correlated with the hydrolysis of adsorbed Zn^{2+}. In addition, the derived adsorption locations and the occupancy factors of both sites from three methods agree well, with some quantitative discrepancies in the minor site location among the XSW, EXAFS, and DFT methods. Additional XSW measurements showed that the adsorption sites of Zn^{2+} were unchanged at pH 6. However, the Zn^{2+} partitioning between the two sites changed substantially, with an almost equal distribution between the two types of sites at pH 6 compared to predominantly monodentate occupation at pH 8.
© 2006 Elsevier Inc. All rights reserved.

1. Introduction

Ion adsorption and electrical double layer (EDL) formation at the oxide-aqueous solution interface are fundamental to a number of processes (Stumm et al., 1992; Brown et al., 1999). Of particular relevance to geochemical systems are the influence of the EDL at mineral-water interfaces on contaminant transport in the subsurface, mineral dissolution and precipitation rates and mechanisms, bioavailability of trace metals, and incorporation of trace metals into growing crystals. While there have been extensive studies of EDL phenomena over the past decades (James and Healy, 1972; Schindler et al., 1976; Benjamin and Leckie, 1981; Kinniburgh and Jackson, 1982; Fokkink et al., 1987; Bedzyk et al., 1990; Hiemstra and Van Riemsdijk,

1996; Venema et al., 1996; Williams et al., 1998; Rietra et al., 1999; Bourikas et al., 2001; Machesky et al., 2001; Sverjensky, 2001), the connection between molecular-scale processes and their macroscopic manifestations has been elusive.

Recent efforts have begun to establish these relationships through coordinated studies of the adsorption of mono-, di-, and tri-valent cations at the rutile TiO_2 (110)-water interface. These studies, making use of high resolution X-ray based structural probes, quantum mechanical calculations, classical molecular dynamics simulations, surface complexation models, and pH titrations of powder suspensions and electrophoresis, have provided new insights into EDL phenomena by directly linking microscopic information to macroscopic properties (O'Day et al., 1996; Towle et al., 1999; Machesky et al., 2001; Fedkin et al., 2003; Bandura et al., 2004; Predota et al., 2004a,b; Zhang et al., 2004a,b; Ridley et al., 2005).

More specifically related to the current study, the effects of solution species and ionic strength on the EDL distribution were also explored for Zn^{2+} and Sr^{2+} ions at the same interface, revealing that the adsorption structures of divalent ions is largely insensitive to changes of background electrolytes on this surface (Zhang et al., 2006). The rutile (110) surface in contact with water consists of a basal plane of O and Ti atoms with overlying rows of terminal O (TO) and bridging O (BO) atoms bonded, respectively, to one or two Ti atoms in the basal plane (Fig. 1a and b). The adsorption of Zn^{2+} at the rutile (110)-water interface is unusual for a number of reasons. First, it was observed to adsorb by a distinctly different mechanism from all other ions investigated (Zhang et al., 2004a,b). Unlike Rb^+, Sr^{2+}, and Y^{3+} which all adsorbed in the same tetradentate site (above a basal plane O atom and bonded to two BO and two TO atoms), Zn^{2+} adsorbs at two distinct sites at pH 8: nominally above the BO site (Fig. 1c, site A_1), and between two TO sites (Fig. 1c, site A_2), with the majority of Zn^{2+} in the A_1 site (Zhang et al., 2004b). Second, the agreement between the experimentally observed ion locations and those predicted by molecular dynamics simulations (Predota et al., 2004b) was excellent for Rb^+ and Sr^{2+}, whereas substantial discrepancies between measured and predicted Zn^{2+} locations existed. While molecular dynamics (MD) simulations of Zn^{2+} at a negatively charged, hydroxylated TiO_2 (110) surface also yielded two adsorption sites around A_1 and A_2, respectively (Predota et al., 2004b; Zhang et al., 2004b), there were substantial disagreements between the density functional theory (DFT) calculations, the MD simulations and X-ray measurement at site A_2, including a discrepancy of ~0.7 Å in the predicted heights above the basal plane. We speculated (Zhang et al., 2004b) that the disagreement might be due to: (1) uncertainties of the XSW measurements or, (2) an implicit assumption in the DFT and MD studies that the surface adsorbed Zn^{2+} species remained sixfold coordinated, as found for aqueous Zn^{2+} (Marcus, 1997; Zhang et al., 2004b) and suggested from EXAFS studies of Co^{2+}
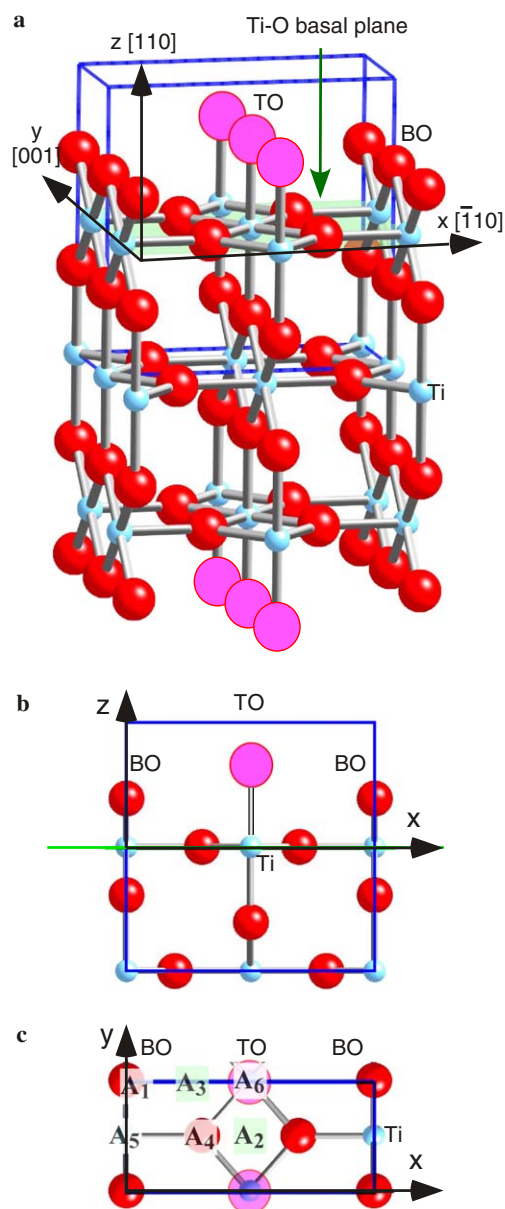

Fig. 1. Rutile TiO_2 (110) surface structure. (a) Perspective view of TiO_2 (110) surface. This also corresponds to the TiO_2 supercell used in DFT calculation. A redefined surface unit cell (in blue) is shown. Shaded plane is defined as Ti–O basal plane. The coordinate system is defined as x, y, z along [$\bar{1}10$], [001], and [110] direction, respectively. (b) Side view, and (c) Top view of the surface unit cell with added TO sites. The nominal adsorption sites, A_1 through A_6, are labeled. For clarity, only atoms at or above the surface basal plane are shown in (c).

adsorption on rutile powder and single-crystal surfaces (O'Day et al., 1996; Towle et al., 1999).

Recent studies show that Zn^{2+} often changes its coordination environment from a sixfold coordination in aqueous solutions to a fourfold coordination on adsorption (Alberts et al., 1998; Trainor et al., 2000; Trainor et al., 2001; Trivedi et al., 2001; Elzinga and Reeder, 2002; Manceau et al., 2002; Waychunas et al., 2002; Roberts et al., 2003; Kosmulski and Maczka, 2004; Lee and Anderson, 2005; Lee et al., 2005). This might also happen at the rutile (110)-

aqueous solution interface and could explain some of the differences between the theoretical and experimental results.

Analysis of Zn^{2+} adsorption on rutile powder suspensions using a multi-site complexation model also suggested surface enhanced hydrolysis of the adsorbed Zn^{2+}, i.e., the formation of $Zn(OH)^+$ species, at the rutile (110)-aqueous solution interface at pHs lower than the aqueous hydrolysis constants of Zn^{2+} (Zhang et al., 2004b). Therefore, we have undertaken a more in-depth investigation with a combination of XSW measurements, polarized surface extended X-ray absorption fine structure (EXAFS) spectroscopy, and DFT calculations to explore the structure of adsorbed Zn^{2+} at pH 8. The new results are consistent to first order with the previous data in terms of the Zn^{2+} locations and occupancies. XSW measurements were also carried out at pH 6 to test the sensitivity of Zn^{2+} adsorption to changes in pH.

2. Materials and methods

2.1. Rutile TiO₂ (110) surface

Rutile (α-TiO$_2$) has tetragonal structure, with lattice parameters $a_0 = b_0 = 4.594$ Å, and $c_0 = 2.959$ Å at $T = 298$ K (Abrahams and Bernstein, 1971; Diebold, 2003). When the rutile (110) surface is immersed into aqueous solution, it is known that both the bridging O (BO) and terminal O (TO) sites are fully occupied through reaction of the rutile surface with water (Figs. 1a and b), as supported by X-ray scattering measurements (Zhang et al., 2004b), DFT calculations (Lindan et al., 1998; Bandura and Kubicki, 2003; Bandura et al., 2004; Zhang et al., 2004b), and MD simulations (Predota et al., 2004a). Comparison of ion adsorption behavior revealed that the surface is best described as having both the BO and TO sites protonated at neutral or acidic pH, corresponding to the dissociatively adsorbed water molecules at the TiO$_2$ (110) surface (Zhang et al., 2004b). This is generally consistent with the proton affinities of the O atoms at BO and TO sites calculated using the revised MUlti-SIte Complexation (MUSIC) model (Hiemstra and Van Riemsdijk, 1996; Machesky et al., 2001) and using DFT-optimized surface bond lengths (Fitts et al., 2005).

A non-primitive surface 3D unit cell is defined with its lattice vectors along the crystallographic directions $[\bar{1}10]$, [001], and [110], respectively, as shown in Fig. 1a so that the results from all three approaches can be compared directly. The surface lattice parameters are $a = c = \sqrt{2}a_0 = 6.497$ Å, and $b = c_0 = 2.959$ Å. The coordinate system is defined with the origin ($x = y = z = 0$) located on the basal plane directly underneath the BO site of an unrelaxed bulk lattice, as shown in Fig. 1. Previous X-ray crystal truncation rod (CTR) measurements and DFT calculations indicate minimal displacements of the basal plane ions from their bulk structural positions (Zhang et al., 2004b). The rectangular

unit shown in Fig. 1c is defined as the rutile (110) surface 2D unit cell, with an area of $6.497 \times 2.959 = 19.22$ Å^2.

There are 6 high-symmetry adsorption sites for inner-sphere adsorbed ions at the rutile (110)-aqueous interface. These adsorption sites (A$_n$, $n = 1$–6, as labeled in Fig. 1c) are characterized by their lateral positions: A$_1$ is monodentate to one BO site; A$_2$ is bidentate to two TO sites; A$_3$ is bidentate to one BO and one TO site; A$_4$ is tetradentate to two BO and two TO sites; A$_5$ is bidentate to two BO sites; and A$_6$ is monodentate to one TO site.

Polished rutile (110) single crystals ($10 \times 10 \times 1$ mm^3) were obtained from Princeton Scientific with a typical miscut of $\leqslant 0.1°$ with respect to the (110) crystallographic plane. The sample preparation procedure and the resulting surface topography, with large atomically flat terraces, are described elsewhere (Zhang et al., 2006).

2.2. XSW measurements

The single crystal Bragg X-ray standing wave (XSW) method is a powerful tool to probe adsorbate positions at the solid–water interface, as reviewed recently (Bedzyk and Cheng, 2002). The principles of the XSW imaging method and its specific application at the rutile–aqueous solution interface can be found elsewhere (Bedzyk and Cheng, 2002; Cheng et al., 2003; Okasinski et al., 2004; Zhang et al., 2004a). Briefly, the fluorescence signal from a specific element and the Bragg reflectivity are measured simultaneously as a function of incident angle of the X-ray beam. The coherent position P_H and coherent fraction f_H of the fluorescing element are directly obtained from the measurements. These two parameters represent the phase and the amplitude of the Hth ($= hkl$) Fourier component of the fluorescing element's spatial distribution (all notations of Bragg planes refer to the bulk crystal lattice structure). As demonstrated recently, the complete density profile (projected into the substrate crystallographic unit cell) can be obtained by a discrete Fourier summation with a full set of Fourier components (Zhang et al., 2004a):

$$\rho(\mathbf{r}) = \sum_H f_H \exp[i(2\pi P_H - \mathbf{H} \cdot \mathbf{r})]$$
$$= 1 + 2\sum_{H>0} f_H \cos[i(2\pi P_H - \mathbf{H} \cdot \mathbf{r})] \qquad (1)$$

Here $\rho(\mathbf{r})$ represents the normalized 3D distribution profile of the fluorescent species ($\int \rho(\mathbf{r})d\mathbf{r} = 1$) and $\mathbf{H} = h\mathbf{a}_0^* + k\mathbf{b}_0^* + l\mathbf{c}_0^*$ is the reciprocal space vector corresponding to the (hkl) Bragg peak. $|\mathbf{H}| = \frac{2\pi}{d_H}$, where d_H is the d-spacing of the (hkl) planes. This spatial reconstruction results in an image with a spatial resolution that is limited by the number of Fourier components included (typically, ~ 1 Å).

Further refinement of the structure is carried out by the traditional XSW triangulation method, where the ion adsorption structures are modeled to reproduce the measured coherent positions and fractions. We use the direct, model independent XSW imaging results as a starting

structure. Sensitivity to the adsorbate position with this approach is ∼0.01 Å.

The XSW measurements were preformed at the Advanced Photon Source (APS), Argonne National Laboratory (ANL). A symmetric Si (111) high heat load monochromator is used to select the X-ray energy of 10.9 keV. One or two sets of double-bounce Si channel cuts are used as the post-monochromator optics to further collimate the beam. The typical beam size was 0.05×0.1 mm^2. The detailed procedures of the Bragg XSW measurements were described elsewhere (Zhang et al., 2006).

The solution was $[ZnTr_2] = 10^{-5}$ mol/kg (molal or m), titrated to pH 6.0 or 8.0 by the addition of HTr (Tr$^-$ is trifluoromethanesulfonate, a synthetic, non-complexing, monovalent anion) and buffered by the addition of sub-millimolal final concentrations of Tris(hydroxymethyl)aminomethane (Tris). At room temperature and these pH's and ionic strengths, the solutions are undersaturated with respect to crystalline ZnO and Zn(OH)$_2$ solid phases, and Zn$^{2+}_{aq}$ is the dominant species in solution (Benezeth et al., 2002; Wesolowski et al., 2004). During the X-ray measurements, the typical solution thickness above the sample surface is estimated to be ∼2–5 μm.

The absolute total adsorbed ion coverage was calibrated by comparing the fluorescence yield to a Zn-ion-implanted standard sample measured in the same experimental geometry. A convenient unit for ion coverage is the monolayer (ML). Here, we define 1 ML as 1 ion per TiO$_2$ (110) surface 2D unit cell area, i.e., 1 ML = 5.3×10^{14} ions/cm^2 = 8.8 μmol/m^2.

XSW measurements are summarized in Table 1 with details on the choice of post-monochromator optics. Two pairs of surface-symmetry equivalent reflections were measured, i.e., (111) and (11$\bar{1}$), (210) and (120), to probe the symmetry of the adsorbate sites. The same coherent frac-

tions and coherent positions for each pair of reflections were obtained within experimental error. This confirms that the adsorbate distribution follows rutile (110) surface symmetry.

2.3. Density functional theory calculation

Plane wave, density functional theory (DFT-PW) calculations were performed on a variety of Zn^2–H$_2$O–TiO$_2$–2OH$^-$ structures to determine the most stable arrangements of Zn^{2+} on the rutile (110) surface. For this purpose, a 3D supercell was created to model the (110) surface, which laterally consisted of 1×2 non-primitive surface unit cells. Three Ti layers (i.e., nine atomic planes) were included in the model slab system, which resulted in the whole unit shown in Fig. 1a. Vertically, the supercell was chosen to be 24 Å, with neighboring (110) surfaces separated by a ∼15 Å vacuum gap. The positions of all atoms were allowed to relax except the positions of the central layer atoms which were fixed at the bulk crystal lattice sites (Bandura et al., 2004). Inversion symmetry was imposed on the positions of all atomic centers to avoid the non-zero dipole moment in z-direction. As a consequence, both sides of the slab had the same structure and composition. The supercell dimensions were kept constant during optimization. The Zn^{2+} surface complexes were added to Ti–O–H surfaces that had been previously energy minimized (Bandura and Kubicki, 2003). Two H$^+$ ions were removed from these simulation cells to keep the overall system neutral.

Minimum energy structures of slab models were determined using the generalized gradient approximation (GGA) of Perdew and Wang (Perdew, 1991) (PW91) calculations within the CASTEP (Segall et al., 2002) module of Cerius^2 (Accelrys Inc., San Diego, CA). Ultrasoft pseudopotentials (Vanderbilt, 1990) were used in most calculations,

Table 1
XSW measurements of Zn^{2+} at the rutile (110)-aqueous solution interface

Reflection ($H = hkl$)	d_H (Å)	$\lvert H \rvert$ (Å^{-1})	PM1	PM2	Zn^{2+}			Ti					pH
					f	P	Θ_{tot} (ML)	f	P	DW	f_{cal}	P_{cal}	
(110)	3.25	1.93	Si (220) 50%	Si (220) 50%	0.59 (1)	1.01 (1)	0.41 (5)	0.95 (1)	1.01 (1)	0.98	0.98	1	8
(111)	2.19	2.87	Si (220) 50%	Si (220) 50%	0.73 (2)	0.53 (1)	0.41 (5)	0.31 (1)	0.75 (4)	0.96	0	—	8
(11$\bar{1}$)	2.19	2.87	Si (220) 50%	Si (220) 50%	0.64 (4)	0.59 (1)	0.41 (5)	0.37 (1)	0.75 (1)	0.96	0	—	8
(210)	2.05	3.06	Si (220) 50%	Si (220) 50%	0.53 (3)	0.57 (1)	0.41 (5)	0.08 (1)	0.70 (1)	0.95	0	—	8
(120)	2.05	3.06	Si (220) 50%	Si (220) 50%	0.60 (3)	0.51 (1)	0.41 (5)	0.09 (1)	0.20 (1)	0.95	0	—	8
(101)	2.49	2.53	Si (220) 50%	—	0.32 (2)	0.91 (2)	0.50 (5)	0.97 (1)	0.92 (1)	0.97	0.97	1	8
(200)	2.30	2.74	Si (220) 50%	—	0.16 (4)	0.89 (4)	0.50 (5)	0.82 (1)	0.99 (1)	0.96	0.96	1	8
(211)	1.69	3.72	Si (220) 50%	—	0.38 (3)	0.89 (2)	0.50 (5)	0.88 (1)	0.99 (1)	0.93	0.93	1	8
(101)	2.49	2.53	Si (220) 50%	—	0.35 (2)	0.90 (1)	0.08 (5)	0.82 (1)	0.98 (1)	0.97	0.97	1	6
(200)	2.30	2.74	Si (220) 50%	—	0.29 (1)	0.89 (1)	0.08 (5)	0.87 (1)	1.00 (1)	0.96	0.96	1	6
(211)	1.69	3.72	Si (220) 50%	—	0.37 (2)	0.85 (1)	0.08 (5)	0.85 (1)	1.00 (1)	0.93	0.93	1	6
(111)	2.19	2.87	Si (220) 50%	—	0.65 (15)	0.69 (3)	0.08 (5)	0.30 (3)	0.75 (3)	0.96	0	—	6
(210)	2.05	3.06	Si (220) 50%	—	0.35 (3)	0.34 (1)	0.08 (5)	0.19 (1)	0.74 (1)	0.95	0	—	6
(110)	3.25	1.93	Si (111) 80%	—	0.50 (5)	0.98 (3)	0.08 (5)	1.00 (1)	1.03 (1)	0.98	0.98	1	6

Post-monochromator (PM) optics and relative tuning; the measured coherent fractions f and coherent positions P for Zn^{2+} ions and Ti atoms (uncertainties in parenthesis); and the calculated coherent fractions and positions for Ti atoms based on the bulk rutile crystal structure. Here, the vibration amplitude $\sigma_H = 0.1$ Å is used for calculating Debye–Waller factors (DW = $\exp(-2\pi^2\sigma_H^2/d_H^2)$) of bulk Ti atom.

allowing us to apply a small plane wave cut-off energy -340 eV. The default CASTEP Monkhorst-Pack scheme (Monkhorst and Pack, 1976) was used for choosing k-points and reciprocal space was sampled by special points set $2 \times 2 \times 1$ resulting in 2 k-points in the irreducible part of Brillouin zone. Default CASTEP criteria as implemented in Cerius[2] 4.9 (Accelrys Inc., San Diego CA) were used for seeking the energy minimum.

The selection of these parameters was justified by performing tests of the stability of the structure and relative energies with increasing the accuracy of the parameters. Increasing the number of k-points from $2 \times 2 \times 1$ to $3 \times 3 \times 1$ in the Monkhorst-Pack scheme led to insignificant variations of the equilibrium geometry (Bandura et al., 2004). The corresponding change in the water adsorption energies was less than 4 kJ/mol. Also, that investigation gave evidence that 340 eV energy cutoff is sufficient to produce the correct relative energies for the different H_2O–TiO_2 structures.

The value of the translation vector of 24 Å provides approximately equal distances (10–12 Å) between the centers of Zn^{2+} in z direction when the 3-Ti-layer slab model was used. The test calculations showed that applied vacuum gap is sufficient to avoid the strong H_2O–H_2O interactions in the adjacent periodic replicas in z-direction. One of the investigated structures (sixfold coordinated Zn^{2+} above the BO) has been calculated in equal surface configurations using two different shifts between the structures on opposite slab faces to check the sensibility of the results on changing the distance between Zn^{2+} in the neighboring periodic images. In those cases, the minimal distance between the centers of Zn^{2+} across the vacuum gap differed by about 1 Å, but the predicted energies coincided to within 1 kJ/mol. It should be noted that the minimal distance between Zn^{2+} in x and y directions is ≈ 6 Å which is insufficient to avoid strong Zn^{2+} and H_2O–H_2O interactions in different surface cells. However, study of the convergence of the results with the cell size is problematic due to the rapidly increasing number of H_2O molecules required to provide solvation around the Zn^{2+} ions.

The number of H_2O molecules was chosen to complete the first hydration sphere of the adsorbed Zn^{2+} ion. At least one bond of the adsorbed cation is occupied by the surface O atom, so a minimum of 5 H_2O molecules were added on each side of the slab to provide the possibility of sixfold coordination of the cation. To satisfy the neutrality condition, terminal hydroxyl groups were attached to the fivefold Ti atoms on each surface (Zhang et al., 2004b). This model is the smallest one that can be used for simulating the adsorption of Zn^{2+} on the rutile (110) surface. As was mentioned above, the effects from the interacting of periodically repeated structures may not be negligible, especially due to presence of localized charged centers on Zn^{2+}. Hence, the relative stability of calculated structure obtained using the 1×2 surface unit cells will be interpreted with caution. However, these artifacts do not affect the comparison of calculated positions with the XSW and EXAFS results.

Energy minimizations for systems with many degrees of freedom usually end in local energy minima (rather than global minima) that are close to the initial geometry point. For this reason, we investigated ten different initial positions of Zn^{2+} on the surface (Table 2) to obtain a sufficiently representative range of conformations for the surface complex. In addition, the Vienna Ab Initio Simulation Package (VASP) (Kresse and Furthmuller, 1996) was used in some instances to ensure that CASTEP results were not influenced by the details of the computational scheme. The VASP calculations were carried out using projector-augmented-wave (PAW) pseudopotentials for core-valence electron interactions and the PBE form of GGA was adopted for the exchange-correlation functionals. The same values of the energy cut-off as were used in CASTEP simulations (340 eV), and a sufficiently large number of NG_i and NG_iF grid-points for the fast Fourier transformations, $NGX = 40$, $NGY = 42$, $NGZ = 150$; $NG_iF = 2NG_i$, $i = X$, Y, Z, have been applied in VASP calculations. The small-core PAW pseudopotential for Ti and Zn atoms with energy cutoff $ENMAX = 275$ and 277 eV, respectively, which explicitly treats 3s and 3p electrons of Ti, and 3d electrons of Zn as

Table 2

Positions of Zn^{2+} and coordinates of the nearest O atoms at the rutile (110)-aqueous solution interface as calculated by DFT

Structure	Zn^{2+} structure		Relative energy (kJ/mol)	Zn^{2+} location (Å)			O location (Å)			
	Site	Coordination number		x [$\bar{1}$10]	y [001]	z [110]	Site	x	y	z
A	A_1	6	0	0.09	0.07	3.41	BO	0.11	−0.07	1.36
B	A_1	5	2	0.34	0.30	3.58	BO	0.08	−0.04	1.35
C	A_1	4	−59	0.19	0.32	3.20	BO	0.05	0.08	1.28
D	A_2	5	−22	3.06	1.25	3.17	TO	3.35	−0.21	1.97
E	A_2	5	−41	3.13	1.01	3.61	TO	3.66	−0.09	2.08
F	A_2	5	49	3.23	1.42	3.02	TO	2.93	−0.08	1.91
G	A_6	4	−49	3.24	0.88	3.57	TO	2.75	−0.16	2.05
H	A_2	4	−115	3.08	1.68	2.98	TO	3.34	0.05	2.00
I	A_4	5	−54	1.64	1.37	2.40	BO	0.12	0.01	1.33
J	A_3	4	−60	1.37	0.10	2.83	BO	0.10	0.06	1.32
C*	A_1	4	−89	0.44	0.55	3.18	BO	0.06	0.07	1.31
J*	A_3	4	−67	1.27	0.14	2.98	BO	0.08	0.02	1.31

The energies are provided relative to the energy of structure A. The nearest surface adsorption site is also listed. Structure C* and J* are derived by re-optimizing structure C and J with VASP and then CASTEP.

valence, has been used. The default break condition for the electronic SC-loop, EDIFF $= 10^{-4}$, was used. Geometry optimizations were carried out until all forces on atoms were less than 0.02 eV/ Å.

2.4. EXAFS measurements

Polarization-dependent Zn K-edge surface extended X-ray absorption fine structure (EXAFS) measurements were performed at beamline 11-ID-D, BESSRC/XOR, of the Advanced Photon Source (APS), located at Argonne National Laboratory (ANL), with the preliminary measurements carried out at beamlines 12-BM (BESSRC/XOR) and X-15A at the National Synchrotron Light Source (NSLS), Brookhaven National Laboratory (BNL). The X-ray beam at beamline 11-ID-D was monochromated with a high-heat-load double-bounce Si (220) crystal. The photon energy was scanned through the Zn K-edge (9.580–10.230 keV). The EXAFS measurements were made with polarized X-rays, with the *E*-field parallel to *x* ($[\bar{1}10]$), *y* ($[001]$), and *z* ($[110]$) directions, respectively. The crystal orientation was determined with three non-collinear Bragg reflections ((110), (200), and (111)), and the incident angle and crystal orientation were controlled precisely with a Psi-C spectrometer. The X-ray beam was incident upon the crystal surface at an angle of $\sim 6°$ to make the geometry directly comparable to the surface-normal XSW measurement. Zn K_α fluorescence signal was collected with a 9-element Ge solid state detector (Canberra®). An X-ray absorption spectrum of a ZnO powder standard was measured simultaneously in transmission mode to obtain a precise energy calibration of the Zn K_α absorption edge (using X-rays that were scattered from the incident beam by a Kapton film) (Cross and Frenkel, 1999). The EXAFS measurements were performed using the same pH 8 solution described in XSW measurements.

The absolute amount of the adsorbed Zn^{2+} at the rutile (110)-aqueous solution interface was measured with X-ray fluorescence and calibrated with a standard of Ga ion implanted Si wafer. X-ray fluorescence confirmed that the surface was clean prior to exposure to Zn^{2+} solution ($<10^{13}/cm^2$ Zn^{2+}). After the exposure to solution, the Zn^{2+} coverage was $3 \times 10^{14}/cm^2$, which is typical for Zn^{2+} adsorption at the rutile (110) surface, as judged by the previous XSW measurements (Zhang et al., 2006). Earlier XSW measurements showed that the partitioning of Zn^{2+} ions between the adsorbed phase and all other components is reproducible and typically >50% of the total Zn^{2+} in the system is expected to be in the Stern layer at the rutile (110)-aqueous solution interface (Zhang et al., 2006).

Several EXAFS energy scans were collected and averaged to increase the signal to noise ratio in the measured spectra. The background was removed using the program Athena (Ravel and Newville, 2005) which is an interface to the IFEFFIT (Newville, 2001) algorithms. The variable Rbkg, which specifies the maximum frequency that can be

included in the background function which is removed from the oscillatory part of the absorption spectrum (Newville et al., 1993), was equal to 1.0 Å for all EXAFS spectra. The theoretical models were constructed using Feff 7.02 (Zabinsky et al., 1995) with the atomic positions for both Zn^{2+} and the TiO_2 surface calculated using the DFT results from this study as initial values.

The EXAFS models are built from scattering paths of the photoelectron that is created during the absorption of an X-ray by the atoms of interest. These paths originate at the absorbing atom, go to one or more neighboring
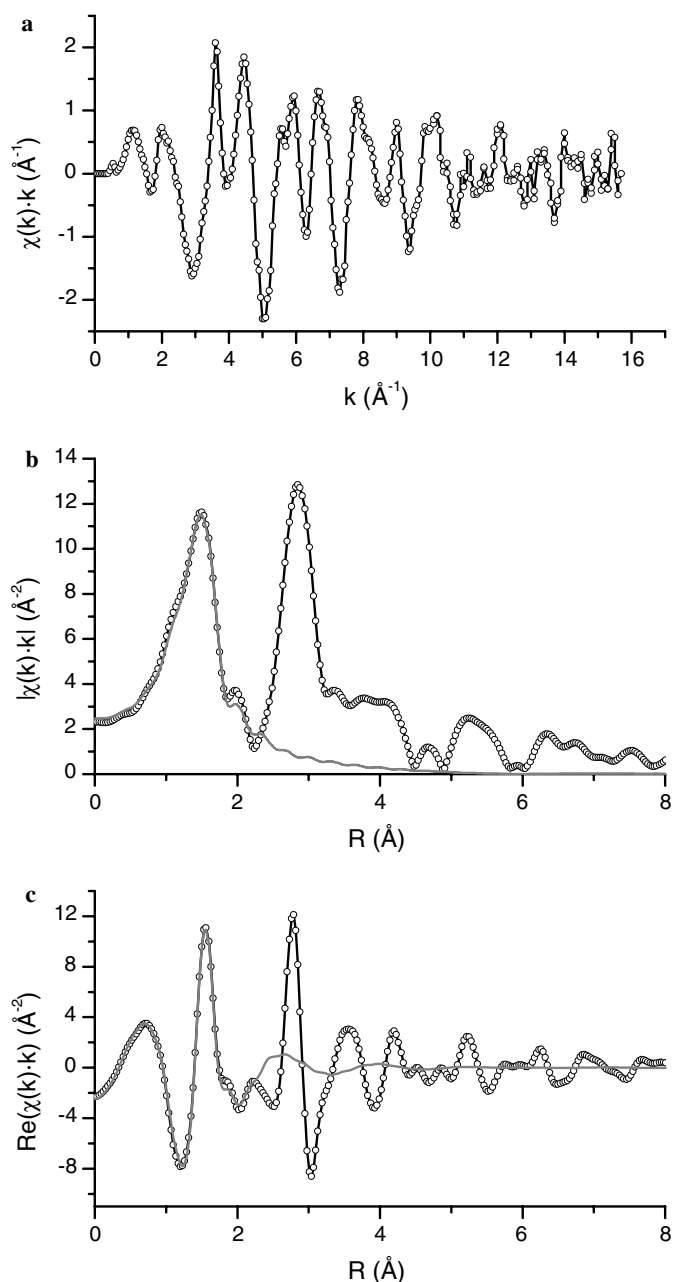

Fig. 2. EXAFS data (open symbol and black line) and fit (solid grey line) from ZnO powder, (a) EXAFS data only, (b) magnitude of the Fourier transform of data and fit, and (c) real part of Fourier transform of data and fit.

atoms and then return to the original absorbing atom. These paths are described in part by the degeneracy of the path, the half path length, and a mean-square displacement of the half-path length, σ^2. For a simple single scattering path, the degeneracy is the number of equivalent atoms in a shell around the absorber, the half-path length is the bond length, and the σ^2 is a measure of the thermal and static disorder in the bond lengths of the atoms.

EXAFS data were collected from a ZnO powder and used to determine an appropriate S_0^2 value. The model is based on the crystal structure of ZnO (Albertsson et al., 1989) with 4 O atoms in the first coordination shell of Zn with an initial Zn–O bond length of 1.974 Å. The data range, k = 2.4 to 12 Å^{-1}, and the fit range, R = 1–2.3 Å result in 10 independent points as defined by the Fourier transformed data range and modeled region of the spectra (Stern, 1993). The model for the first O shell contains four parameters, (change in bond length of -0.010 ± 0.006 Å, σ^2-value of 0.002 ± 0.001 Å^2, energy shift value of -1.5 ± 0.9 eV, and S_0^2-value of 0.89 ± 0.06) (Fig. 2). The fit quality is excellent with an R-factor, representing the average difference between the data and model over the fitted range, of 1%.

3. Results

3.1. XSW results

The measured coherent fractions, coherent positions, and the total coverage of adsorbed Zn²⁺ ions are listed in Table 1. The measured and calculated coherent fractions and coherent positions of bulk Ti atoms are also listed, with calculated values based on the bulk rutile crystal structure. At reflections $\boldsymbol{H}$ = (110), (101), (200), and (211), all Ti atoms are on equivalent atomic planes (i.e., separated by 1 *d*-spacing). The expected Ti coherent positions are 1 (or 0) and the coherent fractions are due to Debye–Waller factors DW = $\exp(-|\boldsymbol{H}|^2\sigma_H^2/2) = \exp(-2\pi^2\sigma_H^2/d_H^2)$, with σ_H the vibration amplitude of the lattice Ti atoms. For simplicity, $\sigma_H = 0.1$ Å is used for all reflections. At reflections $\boldsymbol{H}$ = (111) and (210) (and the symmetry equivalent ones such as (11$\bar{1}$) and (120)), however, the Ti atoms are equally distributed between two atomic planes which are displaced by 1/2 of a *d*-spacing. These two planes destructively interfere, therefore the Fourier component magnitudes (i.e., coherent fractions) for these two reflections are 0, and the phases (i.e., coherent positions) are undefined. The non-zero Ti coherent fractions and 0.75 coherent positions observed for these reflections are due to the under-estimated absolute Bragg peak reflectivity for the less-than-perfect rutile crystal.

The total coverage of Zn²⁺ ions was measured to be 0.08 ML and 0.50 ML, at pH 6 and pH 8, respectively. The fact that a much smaller Zn²⁺ coverage was observed at pH 6 suggests a smaller negative surface charge, which agrees with direct measurements of surface charge from powder titration (Machesky et al., 1998; Machesky et al.,

2001) and second harmonic generation (SHG) (Fitts et al., 2005) measurements. However, previous studies indicate that a single coverage measurement only sets a lower limit on the actual adsorbate saturation coverage, because the coverage of an adsorbate can also be reduced by extrinsic factors, such as surface cleanliness (Zhang et al., 2006).

The Ti atom and Zn²⁺ ion distribution density profiles are generated with the measured coherent fractions and coherent positions according to Eq. (1). Bulk symmetry equivalent reflections are included for imaging Ti atom positions. For instance, ($\bar{1}$10) and (110) are bulk symmetry equivalent reflections; therefore, the Ti coherent fractions and positions should be identical for these two reflections. We find that the rutile (110) surface symmetry is preserved according to our results of Zn²⁺ XSW measurements for surface symmetry equivalent reflections, by comparing the (210) and (120) reflections, and the (111) and (11$\bar{1}$) reflections. Some reflections that are symmetry-related by the bulk crystal structure, such as ($\bar{1}$10) and (110), however, are inequivalent with respect to ion adsorption measurements because they differ in their orientations with respect to the surface (110) plane. The resulting image of Ti atom distribution (Fig. 3a) clearly reproduces the bulk Ti atom arrangements, which implies that the subset of the rutile reflections that we measured are sufficient to obtain a proper element-specific distribution.

The images of the adsorbed Zn²⁺ ion distribution for pH 8 and pH 6 are shown in (Figs. 3b and c), respectively. These two density profiles are similar with respect to their Zn²⁺ locations. The similarity of the Zn²⁺ positions to the derived Ti distribution suggests that the adsorbed Zn²⁺ ions are located close to the projected bulk Ti atom positions, as was also reported for Co²⁺ sorption on rutile surfaces previously (Towle et al., 1999). These two sites correspond to the A_1 and A_2 sites at the rutile (110) surface. These images also directly show that the height of A_2 site above the Ti–O basal plane is significantly lower than that of A_1 site and the occupancies at the two sites are different, especially at pH 8 where Zn²⁺ is predominately adsorbed at the A_1 site. Consequently, the two adsorption sites are inequivalent for adsorbed Zn²⁺ ions, consistent with the surface symmetry.

The spatial resolution of the derived Zn²⁺ distribution profile is approximately 1.6, 1.5, and 1.1 Å along x ([$\bar{1}$10]), y ([001]), and z ([110]) directions, respectively. While these images show the Zn²⁺ profile as a single broad density contour at each of the two adsorption sites, the actual Zn²⁺ distribution could be either a single site at the center of the contour or multiple Zn²⁺ locations distributed within the density contour. Because these features are not resolved by the XSW images, further details of the adsorbed Zn²⁺ ion site distribution were obtained by the traditional XSW triangulation model-fitting method, using these model-independent images as the starting point for optimization. This approach allows us to determine the exact locations and occupation factors (i.e., percentage of Zn²⁺ ions at each site) of the structure, albeit in a model-dependent manner.
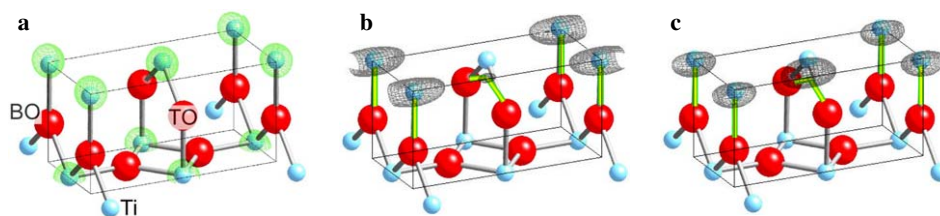
Fig. 3. XSW generated 3D iso-density contour surfaces for (a) Ti atoms, and (b) Zn^{2+} ions at pH 8, and (c) Zn^{2+} ions at pH 6 [(210) reflection excluded]. The iso-density contour surfaces at 65% of the peak element density are plotted overlapping with the reference ball-and-stick model of a half rutile surface unit cell terminated at the Ti–O basal plane. (Note: for clarity, symmetry equivalent densities generated by the bulk rutile translational symmetry are not shown in (b) and (c).)

The basic structural model includes two Zn^{2+} positions, i.e., A_1 and A_2 sites as seen in XSW images. The fitting parameters include the offsets for both Zn^{2+} sites along x, y, and z direction and the occupation factors, respectively. Zn^{2+} ions from disordered sources (e.g., solution ions and/or adsorption on the Kapton window) are parameterized with the ordered fraction, C. The rutile (110) surface symmetry is assumed for structures that nominally break the surface symmetry through equal occupation of symmetrically displaced species. Occupation at one location with the coordinates ($x0$, $y0$, $z0$) by Zn^{2+}, leads to the same amount of Zn^{2+} at positions ($-x0$, $y0$, $z0$), ($x0$, $-y0$, $z0$), and ($-x0$, $-y0$, $z0$).

The best-fit parameters of the model structure at pH 6 and pH 8 are listed in Table 3. Substantial lateral offsets are needed for both A_1 (towards A_3) and A_2 (towards A_4) sites to explain the measured coherent fractions and positions. These results show that the differences between adsorbed Zn^{2+} locations at pH 6 and 8 are insignificant when including the derived uncertainties. The partitioning of Zn^{2+} between A_1 and A_2 sites, however, is sensitive to pH. The derived Zn^{2+} coverage at site A_1 is almost three times as much as that at A_2 at pH 8, whereas the relative coverage of these two sites is comparable at pH 6 (but with a substantially smaller total coverage). This suggests that the relative affinities of the two sites are similar at pH 6 while Zn^{2+} apparently favors the A_1 site at pH 8.

There is one internal inconsistency in the pH 6 data set that should be noted. The measured coherent position for the (111) reflection is $P_{111} = 0.69 \pm 0.03$. Due to the fact that the Zn^{2+} species on the A_1 and A_2 sites are out of phase at this condition, the coherent position is determined by the location of the majority species, so that the A_1 site should have a higher coverage than the A_2 site. Consequently, the (210) reflection is expected to have a coherent position of $P_{210} > 0.50$. However, the measured coherent position for reflection (210) is $P_{210} = 0.34 \pm 0.01$, which suggests that A_2 site should have a higher coverage. This nominal discrepancy was not due to variations in the interfacial structure because repeated measurements of the (111) reflection (including the surface equivalent ($11\bar{1}$) reflection) yielded the same coherent positions within experimental uncertainty at both pH 6 and 8, while repeated measurements of the (210) reflection at pH 8 showed a similar stability. This nominal contradiction concerning the site occupation of the A_1 and A_2 sites at pH 6 derives from a single (210) reflection measured at pH 6 that had relatively poorer statistics and therefore may be unreliable. The XSW triangulation results are, however, only slightly different whether it is included or not. Therefore the derived uncertainties of the structural parameters have been increased to account for this uncertainty, as listed in Table 3. All other combinations of up to 3 out of A_1–A_6 sites were also explored but none of them could explain the XSW data as well as the $A_1 + A_2$ model.

3.2. DFT results

The A_1 site (directly above the BO) is the dominant site for adsorption of Zn^{2+} as seen by the XSW data (Zhang et al., 2004b). The Zn^{2+} adsorption complex was initially modeled (Zhang et al., 2004b) with octahedrally coordinated Zn^{2+} at A_1 site (Fig. 4a) because Zn^{2+} is commonly octahedrally coordinated in aqueous solution (Marcus,

Table 3
Adsorbed Zn^{2+} ion locations and occupation factors of the two Zn^{2+} sites (A_1 and A_2/A_4 sites) at the rutile (110)-aqueous solution interface from XSW and EXAFS measurements, and DFT calculations (with uncertainty in the parenthesis). Structure C* are derived by reoptimizing structure C with VASP and then CASTEP

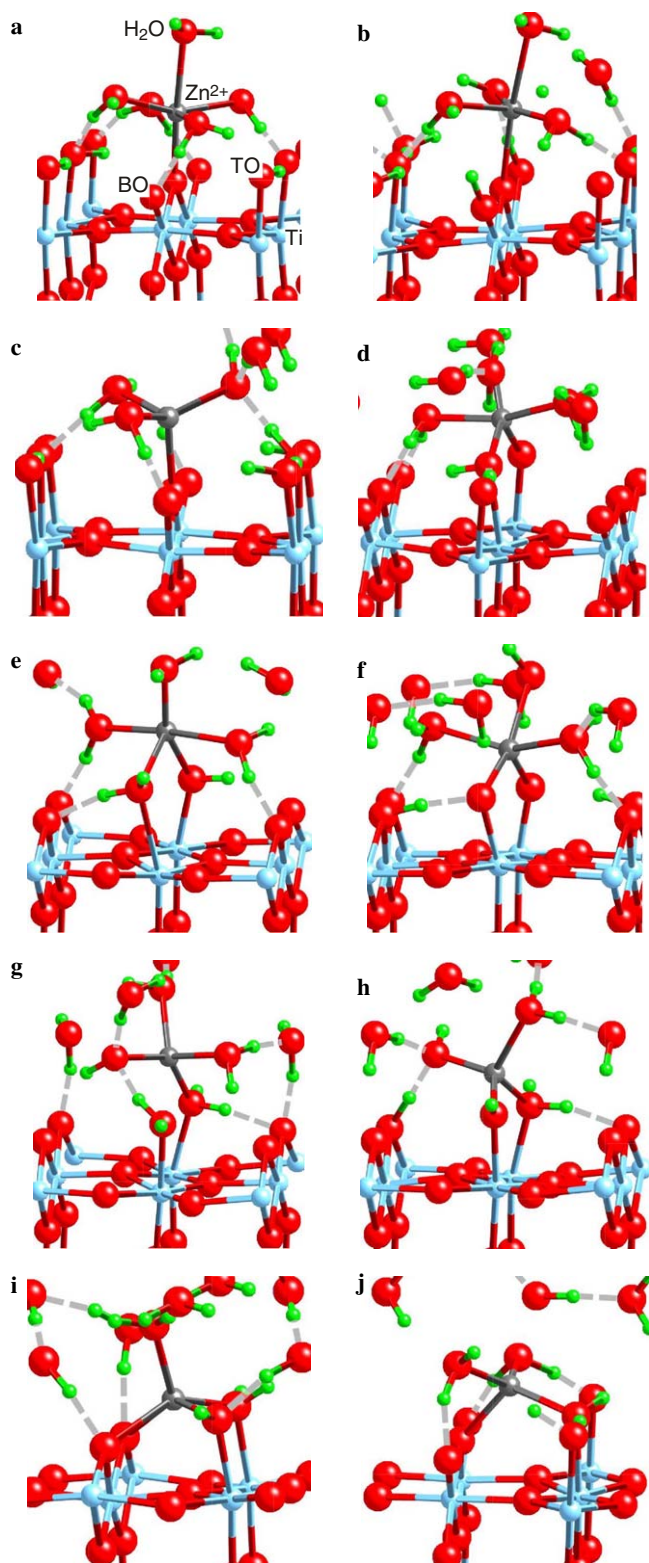|	pH	Site A_1				Site A_2/A_4			
		x (Å)	y (Å)	z (Å)	Occu (%)	x (Å)	y (Å)	z (Å)	Occu (%)
XSW	6	0.19(58)	0.41(15)	3.18(26)	37(13)	2.53(52)	1.48(30)	2.71(12)	30(9)
	8	0.74(6)	0.31(12)	3.23(6)	59(10)	2.64(21)	1.48(47)	2.53(12)	20(6)
DFT		0.19	0.32	3.20	(Structure C)	3.08	1.68	2.98	(Structure H)
		0.44	0.55	3.18	(Structure C*)	1.64	1.37	2.40	(Structure I)
EXAFS	8	0.33(7)	0.43(9)	3.16(9)	41(12)	1.38(21)	0.71(21)	2.51(22)	20(11)

Fig. 4. Structural models of adsorbed Zn^{2+} at the rutile (110)-aqueous solution interface as determined by DFT calculations: adsorption structures of Zn^{2+} at site A_1 are shown as in (a)–(c), at site A_2 or A_6, in (d)–(h), at site A_4, in (i), and at site A_3, in (j). Dashed lines indicate hydrogen bonds.

1997). The positions of five water molecules around the cation did not change significantly during the energy minimization. In the resulting structure, two of the equatorial

H_2O molecules H-bonded with the nearest BO sites, the other two H_2O molecules H-bonded with the surface hydroxyls at TO sites, and the fifth H_2O molecule was directed away from the TiO_2 surface and not H-bonded. Small changes in the initial positions of the cation and H_2O molecules did not produce a noticeably different structure, so the initial configuration can be regarded as relatively stable (Fig. 4a). The minimum energy obtained for this structure will be used as the reference point for energy values reported below for other surface complex configurations (Table 2). (The DFT structures explored are referred hereafter as structures A–J, as shown in Table 2 and Figs. 4a–j, respectively.)

Structure B (Fig. 4b) was obtained by starting with the initial 6-fold coordinated Zn^{2+} in which the position of cation was shifted along x ($[\bar{1}10]$) direction by approximately 1 Å. This configuration had slightly higher energy than that of structure A (Table 2). During the energy minimization, one proton from an H_2O transferred to the nearest BO site, thus producing a hydroxyl group attached to Zn^{2+}. Another H_2O molecule moved away from the cation during the energy minimization, so the coordination number of Zn^{2+} became five.

Another attempt to produce a more favorable fivefold structure in which Zn^{2+} was surrounded by neutral H_2O molecules resulted in a stable fourfold complex with one OH^- group bonded to the Zn^{2+} (Fig. 4c). Again, a proton jumped from an H_2O coordinated to Zn^{2+} to a neighboring terminal hydroxyl on the surface. The energy of the final structure was −59 kJ/mol lower than that of structure A. Therefore, this tetrahedral configuration is predicted to be more stable based on potential energies than the octahedrally coordinated Zn^{2+} species calculated previously (Zhang et al., 2004b). The six to fourfold coordination change should also be favored entropically because release of H_2O from cation coordination results in positive ΔS values (Shock and Koretsky, 1993). In addition, the calculated Zn^{2+} to TiO_2 surface basal plane distance is in better agreement with XSW measurement compared to earlier results. Consequently, other configurations involving tetrahedrally coordinated Zn^{2+} on the surface were investigated.

The second adsorption site on the rutile (110) surface identified by XSW is near the A_2 site, i.e., between two TO sites. Starting with different initial Zn^{2+} positions and surrounding H_2O molecules, the set of structures (Figs. 4d–h) were obtained. Attempts to find a stable, octahedrally coordinated Zn^{2+} failed in this case. In most of the calculated structures, Zn^{2+} has the coordination number 5 (Figs. 4d–f). However, the coordination state is readily converted to an energetically more stable fourfold upon slight perturbation of the structure and further energy minimizations (Figs. 4g and h). The relative energies of these structures are given in Table 2. In structures E, G, and H, an additional hydroxyl at Zn^{2+} was created via the H^+ transfer from a coordinated H_2O to neighboring TO (structures E and G) or BO (structure H) site. Structure H with a bidentate configuration has significantly lower

energy than all other calculated structures (Table 2). Furthermore, the Zn^{2+} height from the Ti–O basal plane differs by only 0.3 Å with respect to XSW result in this case, among the best agreement of the modeled surface complex structures (Table 2). Surprisingly, although structure F predicts a similar Zn^{2+} height, it is the least stable of the tetrahedral complexes based on these potential energy calculations. Thus, a combination of relative energies and comparison to observed structures is employed to determine the configuration of the actual surface complexes.

In addition to two clearly defined adsorption centers obtained from XSW measurements, we have investigated the possibility of Zn^{2+} adsorption in the intermediate positions between the TO and BO sites. Two structures were considered: sites A_4 (Fig. 4i) and A_3 (Fig. 4j). The resulting coordination number of Zn^{2+} are 5 and 4, for structure I and J, respectively, with the calculated energy being slightly more favorable for structure J (Table 2).

Based on these DFT energy minimizations, we conclude that adsorption of hydrated Zn^{2+} cation is accompanied by hydrolysis and the reduction of the coordination number of Zn^{2+} from six to either five or four. This process should be more probable during the adsorption of Zn^{2+} on a negatively charged rutile surface that is probed experimentally, as compared with the neutral surface used in these models.

3.3. EXAFS results

Initially, the polarization-dependent surface EXAFS data were analyzed to determine the O coordination number of Zn^{2+} upon adsorption to the rutile (110) surface. The averaged $\chi(k)$ data are shown in Fig. 5. The low data quality is due to the low concentration of Zn^{2+} ions at the rutile surface. Simple single-shell Zn–O models failed to accurately describe the EXAFS data due to non-Gaussian distribution of Zn–O distances and overlap of neighboring
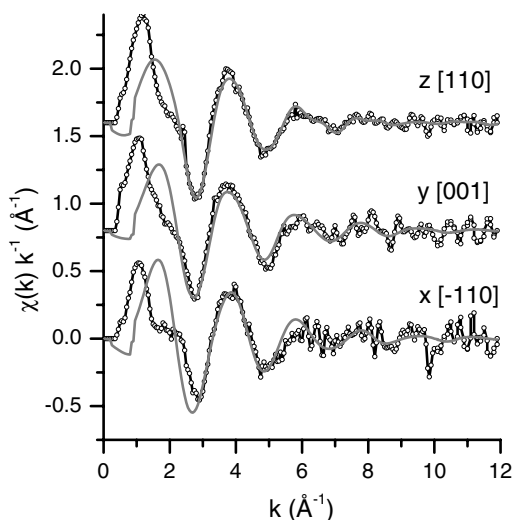

Fig. 5. EXAFS $\chi(k) \cdot k$ (Å^{-1}) data (symbols) and model fit (line) derived from a single-shell fit for the polarization directions along x, y, and z directions, respectively.

Ti signals from the rutile surface. This simple model results in erroneous coordination numbers for O in the range from 8 to 15 with extremely large σ^2 values, representing a highly disordered O shell. A further indication that this simple approach is inappropriate is that it results in a derived Zn–O bond length of 1.99–2.02 Å which is intermediate between the known Zn–O bond lengths of $\sim$1.96 and $\sim$2.10 Å for the four and sixfold coordinated aqueous species. This model is further flawed because the ordered O shell around the Zn^{2+} ions at the rutile surface will have a polarization-dependent coordination number that was not accounted for in the analysis. Specifically, the effective coordination number N_{eff} of a polarized measurement depends on the cosine square of the angle, θ_j, between the polarization vector and the scattering path to the neighboring atoms (with the absorbing atom at the origin), i.e. $N_{eff} = 3\sum_j \cos^2 \theta_j$ (Stohr et al., 1982). Polarization effects for the 1st-shell O and the more distant neighbors are accurately accounted for by specifying the proper polarization dependence in the theoretical FEFF calculation. Consequently, molecular models based on the DFT calculations which give the spatial distribution of the O atoms around the Zn^{2+} serve as useful starting points for accurately fitting the EXAFS data and extracting the needed coordination and structural information.

Based on the XSW results and the DFT calculations, the EXAFS data were analyzed with a mixture of DFT calculated structures and solution Zn^{2+} species, where aqueous Zn^{2+} ions are sixfold coordinated and the Zn–O distance is 2.10 Å. The positions of all atoms in the models were held at the values predicted from the DFT calculations. The only fitting parameters are the relative occupation factors of Zn^{2+} at different surface sites (with aqueous Zn^{2+} making up the remainder) and three σ^2 values (one value for Zn^{2+} to solution O, one for Zn^{2+} to surface O, and one for Zn^{2+} to surface Ti). However, limits of the modeling approach (e.g., limited cell size and solvation, neglect of pH and temperature, inaccuracy of the pseudopotentials in describing H-bonding, etc.) make it impossible to guarantee that the DFT results will exactly mimic experiment. The data contains approximately 7, 7, and 13 independent points as determined from the data and fit ranges listed in electronic annex EA-1-1. All ten energy-minimized configurations from the DFT calculations shown in Fig. 4 were explored and the fitting quickly converged to combinations of structures C, H, I, and aqueous (AQ) Zn^{2+} (electronic annex EA-1-2). Although this model was highly successful in describing the data from the first shell of O atoms contained in the first peak in the Fourier transform of the data, the model failed to reproduce the other features in the data (Fig. 6).

To further refine these structures, the positions of the Zn^{2+} ions on the surface were parameterized in terms of the half-path lengths of all the scattering paths included in the model. This parameterization allows the position of Zn^{2+} to be refined using a minimum of three parameters for each Zn^{2+} position. These models include a total of 13
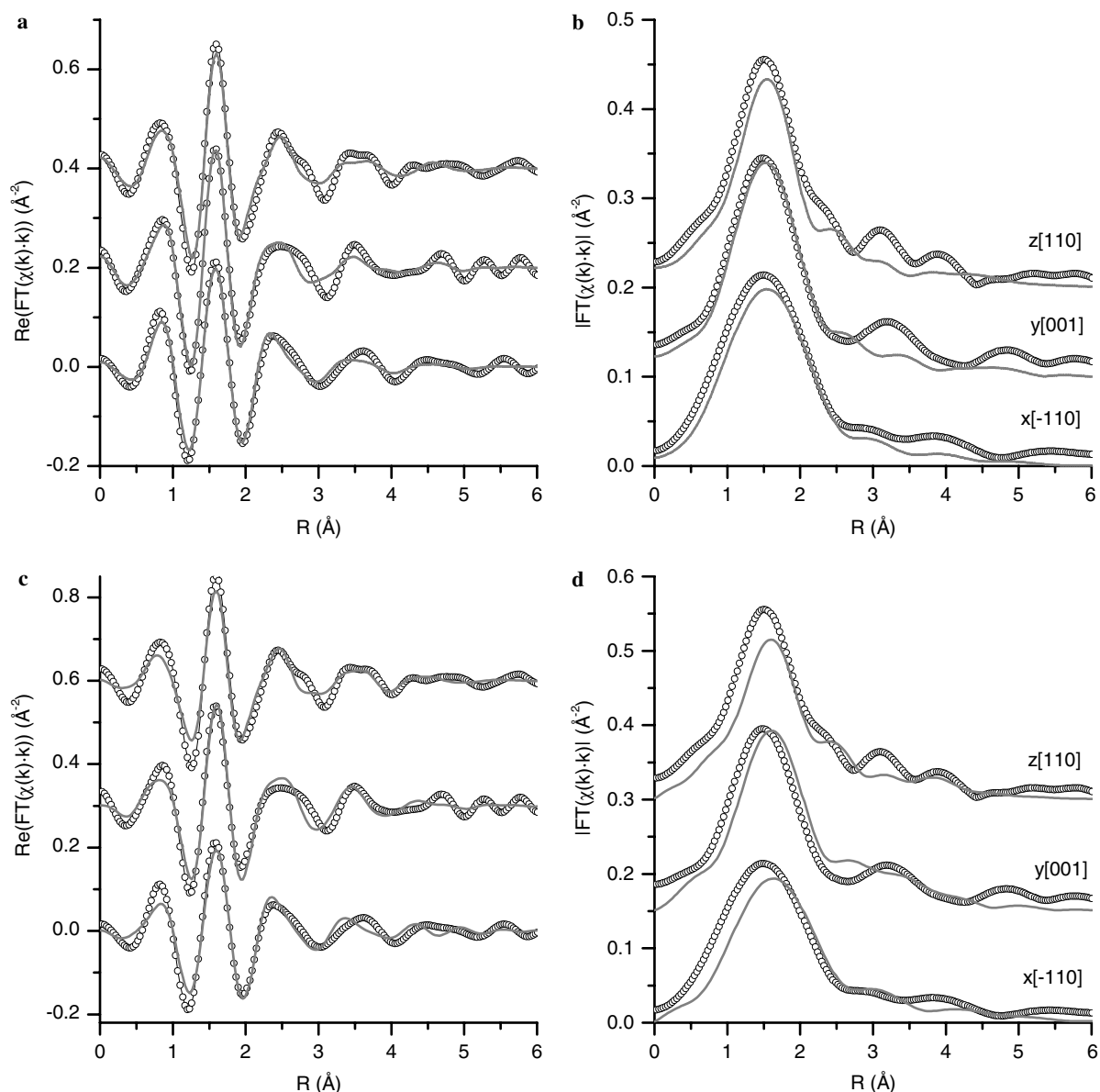
Fig. 6. Fourier transform of the Zn EXAFS data (symbols) are shown as real part (a and c) and magnitude (b and d). Fits to model including the combination of DFT structures C, H, and AQ (a and b) and structures C, I, and AQ (c and d) are also shown. All combinations of sites involving interaction with BO and TO, and coexistence with solution Zn^{2+} were modeled and the reduced-χ^2 compared as listed in electronic annex EA-1-2. The two best-fit models are shown. These models use the atom positions determined from DFT calculation. The percentage of each phase was determined in the fit to the data. The $\chi(k) \cdot k$ EXAFS data for along the *x* (bottom), *y* (middle), and *z* (top) directions is shown in each panel.

parameters; 3 parameters for the *x*, *y*, and *z* positions of (each) Zn^{2+} on the surface at sites A$_1$ and A$_2$/A$_4$, 1 parameter for the distance to all non-surface O atoms bound to the Zn^{2+} ions on the surface, one σ^2-value for the Zn^{2+} to Ti paths, three energy shift values for each polarization-dependent theoretical calculation, and 2 fractional occupancies for surface sites A$_1$ and A$_2$/A$_4$ with the remainder modeled as aqueous Zn^{2+}. The σ^2 values for the aqueous Zn–O paths and for the surface Zn–O paths were held at 0.002 Å^2 as found for the ZnO standard. This parameter was optimized in the fit but was found to be stable at the unrealistic value of zero with an uncertainty that was consistent with the aqueous Zn–O value. A total of 27

independent points for the simultaneous fit to all three data sets is sufficient to refine 13 parameters required for the models.

Fig. 7 shows the local structure of Zn^{2+} in DFT structures C, H, and I with atomic labels used to describe the scattering paths used in the model and listed in electronic annex EA-1-3. The model C–I–AQ is statistically a better match to the data than model C–H–AQ with a reduced-χ^2 value that is approximately two times smaller. In addition, the heights for the Zn^{2+} atom above the surface and the occupancy fractions are in better agreement with the XSW results for the C–I–AQ model than for C–H–AQ model. There is an excellent agreement between the refined
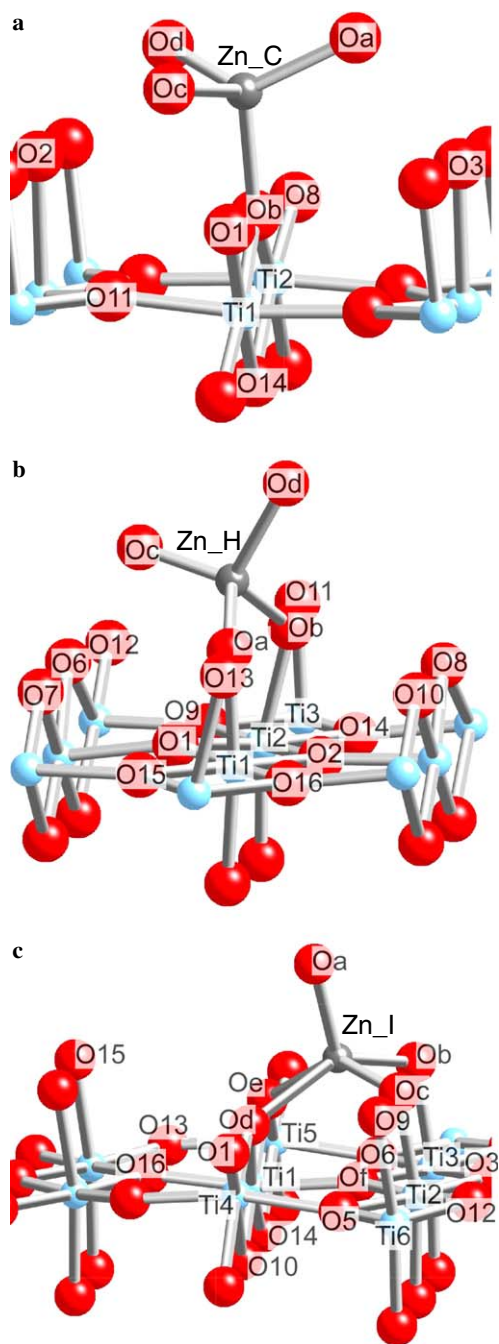
Fig. 7. Models of EXAFS-optimized Zn^{2+} ion locations derived from the DFT calculated structures (a) C, (b) H, and (c) I. The atom labels correspond to the path labels used in the EXAFS model as listed in electronic annex EA-1-3 and EA-1-4.

C–I–AQ model (Table 3 and electronic annex EA-1-4) and the EXAFS data throughout the fit range from 1 to 4 Å (Fig. 8). The derived Zn^{2+} position from EXAFS data for the minor site at pH 8 (Table 3) are between the DFT positions I and J, i.e., around site A_4. The EXAFS model for the minor site is based on the DFT structure I, which is fivefold coordinated. The EXAFS spectra were not reproduced starting with structure J, which is fourfold coordinated. Note that the site A_4 is approximately equiv-

alent to the tetradentate site favored by all other ions, including the alkali and alkaline-earth cations and Y^{3+} investigated by this group (Predota et al., 2004b; Zhang et al., 2004b).

4. Discussion

These results demonstrate that the adsorption of Zn^{2+} at the rutile (110)-aqueous solution interface is unlike that of other ions that have been studied (e.g., Rb^+, Sr^{2+}, and Y^{3+}) where a single adsorption site was observed and there was no apparent change in the ion coordination shell relative to that of the aqueous ion. Instead, the combination of XSW, EXAFS, and DFT results clearly shows that Zn^{2+} adsorbs to rutile in two distinct sites, with an O coordination shell that is perturbed from the octahedrally coordinated geometry in solution, and the adsorption coincides with sorption-induced hydrolysis of the Zn^{2+} ion. Surface-enhanced hydrolysis was also found beneficial in fitting pH-titration and sampling studies of rutile powder suspensions using a Guoy–Chapman–Stern site complexation model (Zhang et al., 2004b).

There is good agreement between the locations of Zn^{2+} at the rutile (110)-aqueous solution interface derived by EXAFS, XSW, and DFT (Fig. 9). The occupation fractions for sites A_1 and A_2 from EXAFS and XSW are in excellent agreement (Table 3), with both showing the A_1 site as dominant with ~2/3 of the specifically adsorbed Zn^{2+}, and ~20% of the total Zn being disordered or characteristic of the solution species. In addition, the precise heights derived for Zn^{2+} agree very well. Zn^{2+} in the A_1 site is at heights of 3.23 ± 0.06 Å and 3.16 ± 0.09 Å, and Zn^{2+} in the A_2/A_4 site is at heights of 2.53 ± 0.12 Å and 2.51 ± 0.22 Å for XSW and EXAFS (Table 3), respectively.

The dominance of the A_1 site is also consistent with the proton affinities of the bridging and terminal O atoms predicted from the revised MUSIC model (Hiemstra and Van Riemsdijk, 1996; Machesky et al., 2001) when DFT Ti–O bond lengths are used (Fitts et al., 2005). These calculations indicate that the bridging O is either bare or singly-protonated at near-neutral pH's, while the terminal O is either singly, or doubly protonated (equivalent to an associated water molecule) at all pH's. Though the deprotonation constants are within 1.5 pH units of one another, the proton bound to the bridging O is more acidic and more labile than the second proton on the terminal O. As can be seen in Fig. 4, the energy-minimized structure C involves a fully deprotonated bridging O, while structures H and I involve two terminal O atoms with one or two bound protons. With increasing pH, the DFT-optimized MUSIC model predicts that there will be more fully deprotonated bridging O atoms available for binding Zn^{2+} than deprotonated terminal O atoms. Furthermore, it is clear from Fig. 4 that binding of Zn^{2+} to two terminal O atoms that also have bound protons requires a coordinated rearrangement of Ti–O bond angles and
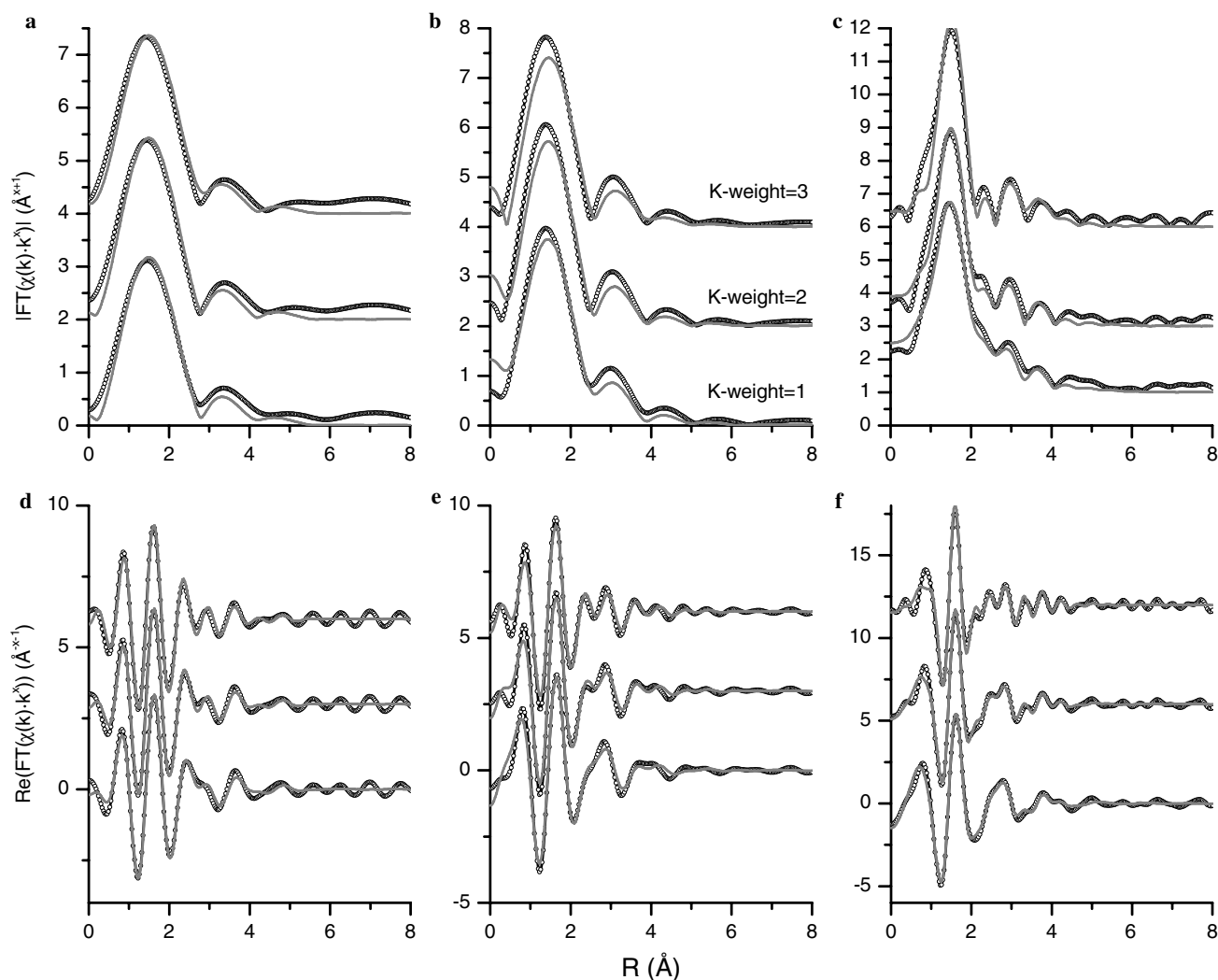
Fig. 8. Magnitude (a, b, and c) and Real parts (d, e, and f) of the Fourier transform of the EXAFS data (symbols) and model fit (line). The model was optimized to the data processed with k-weighting in the Fourier transform of 1, 2, and 3. The k-weight 1 and 2 data is multiplied by 15 and 4, respectively, to rescale to the k-weight 3 data. The first (a and d), second (b and e), and third (c and f) columns correspond to the polarization-dependent data and model fit along x, y, and z directions, respectively. This model represents the best fit to the EXAFS data. The model is based on a mixture of Zn^{2+} coordination environments from the DFT structures C, and I and solution Zn^{2+}. The position of Zn^{2+} on the rutile surface and the percentage of each Zn environment were optimized in the fit to the data, as indicated in Fig. 7. The fit results are listed and compared with DFT and XSW results in Table 3.

shifts of the bound protons away from the sorbing Zn^{2+}, whereas bonding atop the bare BO requires essentially no additional surface rearrangement. Finally, the DFT calculations (Bandura et al., 2004) assign significantly higher negative charge to the bare bridging O than to the singly protonated terminal O. Thus, from both entropic and electrostatic considerations, it is reasonable to expect the A$_1$ site to be favored, relative to the A$_2$ site, particularly with increasing pH.

The primary discrepancies between the XSW, EXAFS, and DFT studies involve the lateral Zn^{2+} positions for the two sites. While all the techniques see substantial displacements along the x direction (i.e., perpendicular to the BO and TO rows), the XSW, DFT, and EXAFS results appear to maintain the optimized Zn^{2+} position with minimal displacements along the y direction for the A$_1$ site. The EXAFS results show the largest displacements along

the y direction for the A$_2$ site. For the A$_1$ site, there is a difference in optimized positions of 0.4 Å along the x direction, which is somewhat bigger than the derived errors and with a somewhat larger discrepancy between DFT and XSW results. The differences between the EXAFS result as compared to the DFT position for A$_1$ site are $\sim$0.10 Å in all directions, which is similar to the uncertainties of the EXAFS measurement. The largest discrepancy is found, however, for the Zn^{2+} position at the A$_2$/A$_4$ site, which differs between XSW and EXAFS results by 1.30 Å along the x-axis, with the DFT structure H a better match to the XSW results in term of the lateral position, but structure I a better match to the EXAFS results (Table 3 and Fig. 9).

A simulated XSW image based on the optimized EXAFS positions shows only a single component at the A$_1$ site which is inconsistent with the image (Fig. 3) obtained
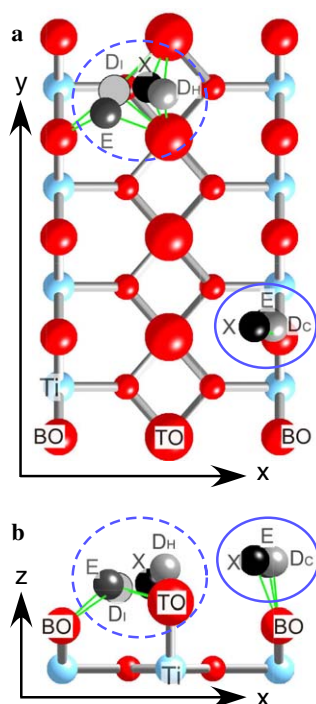
Fig. 9. Comparison of derived Zn^{2+} positions on the rutile (110) surface with the three approaches. Zn^{2+} is shown in the A_1 site (the solid circle) and A_2/A_4 sites (the dashed circle), respectively in (a) top view and (b) side view of the rutile (110) surface. The optimized Zn^{2+} locations for the XSW, EXAFS, and DFT results are labeled with X, E, and D (D_C, D_H and D_I indicate the DFT structures C, H, and I), respectively.

directly from XSW measurements. This is not surprising because both of the EXAFS sites are similar to the XSW derived A_1 site. Similarly, EXAFS calculations based on the XSW results could not reproduce the polarization-dependent EXAFS data. This suggests that there is a contradiction between the XSW and EXAFS results on this aspect of the structure. The main issue with the EXAFS model based on the XSW derived A_2 position is the short Zn^{2+} to TO bond lengths (as discussed previously). We relaxed these TO positions within our EXAFS model, but were unable to reproduce the measured spectra suggesting that this difference is not due solely to structural displacements of the TOs upon adsorption of Zn^{2+}. The discrepancy in the lateral positions for the minor Zn^{2+} site (A_2/A_4) is not understood but may arise from measurement uncertainties (see below) or assumptions within the EXAFS model.

XSW data analysis derived a Zn^{2+} ion height at the A_2 site lower than would naively be expected, which is the major discrepancy between the XSW measurement and the DFT structure H. According to the X-ray crystal truncation rod measurement and DFT calculations, the relaxations of the surface O sites are minimal when the rutile (110) surface is in contact with aqueous solution. This leads to an unusually short Zn–O bond length of ~1.7 Å. However, the TO position is not directly measured at the Zn/TiO_2 (110) interface with XSW. On the other hand, the XSW resolution along x direction is only 1.6 Å, which

makes the model determined Zn^{2+} lateral position less reliable. The bond length would be more realistic if Zn^{2+} were displaced away from the A_2 site along x direction (i.e., towards the A_4 site), or if there were substantial displacement of the surface O locations due to bonding with Zn^{2+}, as seen in some of the DFT optimized structures (e.g., Fig. 4h).

In comparing these results, we note that the DFT calculations were performed for a small simulation cell and did not consider the influence of pH or water molecules in bulk aqueous solution. This might explain the lower calculated energies in DFT calculations of Zn^{2+} at the A_2 site rather than the A_1 site, which contrasts with the experimentally observed larger occupation factor at site A_1 at pH 8 in both XSW and EXAFS. The discrepancy could be because the DFT calculations were done for a charge-neutral surface whereas XSW measurements were carried out on a negatively charged surface. Further calculations combined with molecular dynamic (MD) simulations may yield detailed insights. Including the adsorption of Zn^{2+} at both sites in the same DFT calculation with a larger slab could help probe any interactions between adsorbed Zn^{2+} ions at the two sites. In spite of these significant limitations, we find that the dominant species is correctly predicted by DFT calculations to be the lowest energy structure for adsorption in the A_1 site, and that the minority species in the A_2/A_4 site is found to be one of the lowest energy structures for Zn^{2+} ions interacting with the TO's. While the lowest energy structure at the A_2 site (structure H, Table 2) is found to be in quantitatively poorer agreement with respect to the model-optimized EXAFS data, the absolute difference between the predicted location and that observed independently by XSW is similar to the discrepancy between structure I and the XSW results, albeit with the differences mostly in the vertical and lateral positions, respectively.

To check the reproducibility of the DFT results, the most important structures were re-optimized starting from the final structures listed in Table 2, using VASP (Kresse and Furthmuller, 1996). (Note: VASP was used as an alternative to CASTEP here to generate different initial structures. The VASP results were obtained after most of the CASTEP calculations were complete, so we report only CASTEP results here for consistency.). Those structures that transformed to another (deeper) minimum were re-optimized by CASTEP (using the same approach and unit cell as described in Section 2). As a result, two structures were refined. Structure C has a significantly lower energy: -89 kJ/mol instead of -59 kJ/mol, which implies the increased importance of A_1 site with respect to A_2/A_4 site. Structure J also has a slightly decreased the energy from -60 to -67 kJ/mol, and it is accompanied by the hydrolysis of one attached water. The two structures, labeled as structure C^* and J^*, are also listed in (Tables 2 and 3). The slight changes of the Zn^{2+} coordination environments in C^* and J^* do not affect the qualitative results of the EXAFS component analysis, as listed in electronic annex

EA-1-2. The final best fit results should have no essential change from the C–I–AQ combination as shown in Table 3 when Relaxation of Zn^{2+} positions allowed.

We looked into the possibility of the polynuclear Zn^{2+} species forming at the interface, as a possible explanation for the ~20% of the Zn^{2+} that is not coherently bound at the surface. Attempts to include Zn^{2+} as a second shell contribution to the EXAFS data failed to improve the quality of fit. The surface coherent coverage of Zn is estimated to be 0.3 ML (~3 μmol/m^2) at pH 8, which is smaller than the saturated coherent coverage we found earlier (Zhang et al., 2006). Because this saturated coherent coverage is comparable with the estimated coverage based on close-packing of hydrated ions (Zhang et al., 2006), it is reasonable to believe that the Zn^{2+} adsorbs primarily as mononuclear species at rutile (110)-aqueous solution interface. On the other hand, our earlier observation showed that Zn loading increased with extended X-ray exposure, which leads to a decreasing Zn coherent fraction (Zhang et al., 2006). This may indicate surface induced Zn^{2+} precipitation under those circumstances. In contrast, Zn coverage remained stable which suggests beam induced damage was minimal during our most recent measurements.

Normally Zn^{2+} is found in either fourfold (e.g., ZnO) or sixfold (e.g., Zn$^{2+}_{aq}$, ZnCO$_3$) first-shell O coordination environments (and less commonly in fivefold coordination environments). Zn^{2+} has been reported to change coordination from a sixfold coordinated aqueous species to a fourfold species upon sorption to (hydr)oxide surfaces (Trainor et al., 2000; Trainor et al., 2001; Trivedi et al., 2001; Elzinga and Reeder, 2002; Manceau et al., 2002; Waychunas et al., 2002; Roberts et al., 2003; Kosmulski and Maczka, 2004; Lee and Anderson, 2005; Lee et al., 2005) or to bio-ligands (Alberts et al., 1998). This transformation has been observed to happen in two situations, inner-sphere adsorption and precipitation. In precipitation (or coprecipitation), the Zn^{2+} coordination is determined by the structures of precipitates. For instance, when amorphous Zn(OH)$_2$ precipitates, fourfold coordinated Zn was observed (Roberts et al., 2003). On the other hand, when inner-sphere adsorption occurs, any preference that Zn^{2+} shows for a fourfold coordination would likely depend on the detailed structure and protonation state of the surface ligands, which in turn depend on substrate and solution conditions.

Although it is widely believed that the dominant species in the aqueous solution at pH < 8 is sixfold coordinated, DFT calculations show that the energy difference between the fourfold and sixfold Zn^{2+} species in the gas phase are minimal (Pavlov et al., 1998). There are also suggestions that the reduced dielectric constant could enhance the transformation of aqueous species from sixfold to fourfold because lower dielectric constants favor ion pairing and smaller charges (Dudev and Lim, 2000). The dielectric constant may be lower near the oxide-aqueous solution interface than that in the bulk solution (Brown et al., 1999; Zhang et al., 2004b), although the magnitude of the inter-

facial dielectric constant and its spatial extent into solution are not well understood.

Based on MUSIC model fitted Stern-layer capacitance values from powder titration measurements and the XSW measured Zn^{2+} height above the rutile (110) surface, the Stern-layer dielectric constant appropriate for Zn^{2+} is about 50 (Machesky et al., 2001; Zhang et al., 2004b). Moreover, a limited extent of water dipole ordering (within 15 Å of the rutile surface) is found from X-ray reflectivity and MD simulations. Therefore, it is reasonable to infer that the adsorbed Zn^{2+} will be in a lower dielectric environment than bulk solution. Another contributing factor may be the local charge distribution. It has been proposed that the negatively charged ligand(s) could enhance the stability of the fourfold coordination geometry because strong OH$^-$ ligands have shorter metal–O bond distances which lengthens the remaining metal–O bond lengths to the associated H$_2$O molecules (Dudev and Lim, 2000; Manceau et al., 2002). Such observations are consistent with bond valence theory, where the change in bond valence due to the substitution of a H$_2$O by a surface O ligand would favor fourfold coordination. That these dielectric and charge distribution effects are significant enough to alter Zn^{2+} surface coordination from that observed in bulk solution is not surprising given the relatively small energy differences between the octahedral and tetrahedral coordination environments.

The hydrolysis of metal ions upon adsorption has been suggested in many previous macroscopic and spectroscopic studies (James and Healy, 1972; Schindler et al., 1976; Benjamin and Leckie, 1981; Kinniburgh, 1983; Lowson and Evans, 1984; Spark et al., 1995; Miyazaki et al., 1996; Trainor et al., 2000; Hiemstra and Van Riemsdijk, 2002; Roberts et al., 2003; Peacock and Sherman, 2004), and surface induced hydrolysis is a common and successful construct in Surface Complexation Models (Criscenti and Sverjensky, 2002; Ridley et al., 2005). However, an integrated approach is needed to confirm that hydrolyzed surface structures do indeed exist. X-ray based measurements can derive the adsorption structure but are insensitive to whether a first shell O atom exists as in a water molecule or a hydroxyl group. Bond valence theory is not definitive enough by itself to determine whether hydrolysis occurs for an adsorbed species (Trainor et al., 2000). With the atomic level knowledge from the XSW measurements, a Gouy–Chapman–Stern surface complexation model predicted that the surface induced hydrolysis would happen at the rutile (110)-aqueous solution interface upon Zn^{2+} adsorption, (Zhang et al., 2004b). The present DFT calculations, in combination with the XSW and EXAFS measurements, confirm the hydrolysis of Zn^{2+} upon adsorption and that the transformation of water to hydroxyl in the Zn^{2+} coordination shell is directly coupled to the loss of O atoms from the first coordination shell of the sixfold coordinated solution Zn^{2+} species.

Based on this integrated set of observations, we can speculate what happens when Zn^{2+} adsorbs to rutile (110)-aqueous interface. The X-ray measurements (Zhang

et al., 2004b), DFT calculations (Lindan et al., 1998; Zhang and Lindan, 2003a,b), and molecular dynamic simulations (Predota et al., 2004a,b) all showed that the first few adsorbed water layers on the rutile (110) surface are highly constrained and oriented. This leads to a dielectric constant at the interface that is lower than in the bulk solution, as suggested in many previous investigations of surface adsorption phenomena (Brown et al., 1999; Teschke et al., 2000). When a hydrated $Zn(H_2O)_6^{2+}$ ion adsorbs under the effects of a lower interfacial dielectric constant and a locally charged interfacial ligand(s), the first shell coordination is reduced to four or fivefold by dehydration. At the same time, hydrolysis of Zn^{2+} ion would reduce the overall charge of the adsorbed group; thereby lowering the free energy, especially in a region where the dielectric constant is lower than in bulk aqueous solution. This is consistent with studies that have suggested that the dehydration process could be accompanied by proton transfer, i.e., hydrolysis occurs (Peschke et al., 1999; Shvartsburg and Siu, 2001) in the gas phase when the coordination number of Zn^{2+} is less than 6. Although the environment of a hydrated interface is different from that in the gas phase (e.g., with a higher dielectric constant and a hydrogen bonding network), similar coupling of the dehydration and proton transfer processes could be occurring during the adsorption of Zn^{2+} on rutile as well.

5. Summary

Adsorption of Zn^{2+} at the rutile TiO_2 (110)-aqueous solution interface was investigated by XSW measurements, DFT calculations and polarization-dependent surface EXAFS measurements. XSW measurements show that while Zn^{2+} adsorption sites are insensitive to pH in the range of 6–8, the partitioning of Zn^{2+} between the two sites and the coherent coverage change substantially.

The adsorption position with the lowest energy among the various configurations explored with DFT calculations is for structure H (A_2 site), in which Zn^{2+} is adsorbed between two TO sites (relative energy −114 kJ/mol). The next group of lowest energy configurations, includes 5 (i.e., structures C, E, G, I, and J) of the 10 attempted structures spanning all configurations tested.

The XSW measured Zn^{2+} positions are on top of a surface BO site (site A_1) and bridging between two TO sites (site A_2). The closest matches from the DFT determined positions are the structure C (site A_1) and structure H or I (site A_2/A_4).

Polarization-dependent surface EXAFS measurements at pH 8 are interpreted with a mixture of the adsorbed Zn^{2+} at two different sites plus the aqueous Zn^{2+} species which is fully consistent with XSW results. The occupancy factors of Zn^{2+} adsorbed at the different sites and the height of the Zn^{2+} ions above the rutile surface also agree very well with the XSW measurements. The derived adsorption sites, however, show discrepancies between the XSW and EXAFS in terms of the detailed lateral

adsorption position. The dominant EXAFS site matches closest with the DFT structure C which is similar to the XSW A_1 site. All three measurements (DFT, EXAFS, and XSW) converge well for this site as demonstrated in Fig. 9, and molecular dynamics simulations indicate a similar sorption geometry for the dominant site (Predota et al., 2004b). Despite the quantitative differences in the lateral positions of the Zn^{2+} minor species determined by XSW, DFT, and EXAFS, all of the results reveal that the adsorption site is between A_2 and A_4. It is possible that although the Zn^{2+} ion cannot simultaneously bond to the two TO and BO sites in the tetradentate site because of its smaller ionic radius, it may favor a similar geometry by shifting from the A_2 site towards one of the neighboring TO sites. The same behavior has been observed (M. Predota, personal communication, 2005) for Li^+ at the rutile (110) surface in preliminary MD simulations using the same model described previously (Predota et al., 2004a,b). Bare Zn^{2+} and Li^+ have similar ionic radii, 0.75 and 0.69 Å, respectively (Marcus, 1997), making them too small to contact all four O atoms in the tetradentate site favored by larger ions.

The DFT calculations are in agreement with the XSW and EXAFS results for the dominant site at pH 8 that predict that Zn^{2+} ions is fourfold coordinated and hydrolyzed, which is significantly different from the typical Zn^{2+} species in the aqueous solution. The minor site at pH 8 is predicted to be either four or fivefold coordinated; in either case the Zn^{2+} ions are hydrolyzed at this site as well.

These results demonstrate that a multi-technique approach, including structural and spectroscopic measurements and high level DFT theory, allow for a complete characterization of the adsorption of ions at the oxide-water interface, even when the actual structure involves multiple adsorption sites, changes in the ion hydration shell structure, as well as hydrolysis of the adsorbed species. Comparison of such results with macroscopic pH-titration/adsorption studies of powder suspensions and large-scale molecular dynamics simulations can lead to definitive information on the molecular structure of sorbed species at the oxide-water interface, as well as realistic models to rationalize and accurately predict the macroscopic manifestations of ion adsorption phenomena.

Associate editor: James R. Rustad

Appendix A. Supplementary data

Supplementary data associated with this article can be found, in the online version, at doi:10.1016/j.gca.2006.06.325.

References

Abrahams, S.C., Bernstein, J.L., 1971. Rutile: normal probability plot analysis and accurate measurement of crystal structure. *J. Chem. Phys.* **55**, 3206–3211.

Alberts, I.L., Nadassy, K., Wodak, S.J., 1998. Analysis of zinc binding sites in protein crystal structures. *Protein Sci.* **7**, 1700–1716.

Albertsson, J., Abrahams, S.C., Kvick, Å., 1989. Atomic displacement, anharmonic thermal vibration, expansivity and pyroelectric coefficient thermal dependences in ZnO. *Acta Crystallogr. Sec. B: Struct. Sci.* **45**, 34–40.

Bandura, A.V., Kubicki, J.D., 2003. Derivation of force field parameters for TiO₂–H₂O systems from ab initio calculations. *J. Phys. Chem. B* **107**, 11072–11081.

Bandura, A.V., Sykes, D.G., Shapovalov, V., Truong, T.N., Kubicki, J.D., Evarestov, R.A., 2004. Adsorption of water on the TiO₂ (rutile) (110) surface: a comparison of periodic and embedded cluster calculations. *J. Phys. Chem. B* **108**, 7844–7853.

Bedzyk, M.J., Bommarito, G.M., Caffrey, M., Penner, T.L., 1990. Diffuse-double layer at a membrane-aqueous interface measured with X-ray standing waves. *Science* **248**, 52–56.

Bedzyk, M.J., Cheng, L.W., 2002. X-ray standing wave studies of minerals and mineral surfaces: principles and applications. In: Fenter, P., Rivers, M.L., Sturchio, N.C., Sutton, S.R. (Eds.), *Reviews in Mineralogy and Geochemistry, Vol. 49: Applications of Synchrotron Radiation in Low-Temperature Geochemistry and Environmental Sciences*. MINERALOGICAL SOC AMERICA, Washington, pp. 221–266.

Benezeth, P., Palmer, D.A., Wesolowski, D.J., Xiao, C., 2002. New measurements of the solubility of zinc oxide from 150 to 350 °C. *J. Solution Chem.* **31**, 947–973.

Benjamin, M.M., Leckie, J.O., 1981. Multiple-site adsorption of Cd, Cu, Zn, and Pb on amorphous iron oxyhydroxide. *J. Colloid Interf. Sci.* **79**, 209–221.

Bourikas, K., Hiemstra, T., Van Riemsdijk, W.H., 2001. Ion pair formation and primary charging behavior of titanium oxide (anatase and rutile). *Langmuir* **17**, 749–756.

Brown, G.E., Henrich, V.E., Casey, W.H., Clark, D.L., Eggleston, C., Felmy, A., Goodman, D.W., Gratzel, M., Maciel, G., Mccarthy, M.I., Nealson, K.H., Sverjensky, D.A., Toney, M.F., Zachara, J.M., 1999. Metal oxide surfaces and their interactions with aqueous solutions and microbial organisms. *Chem. Rev.* **99**, 77–174.

Cheng, L., Fenter, P., Bedzyk, M.J., Sturchio, N.C., 2003. Fourier-expansion solution of atom distributions in a crystal using X-ray standing waves. *Phys. Rev. Lett.* **90**, 255503–255504.

Criscenti, L.J., Sverjensky, D.A., 2002. A single-site model for divalent transition and heavy metal adsorption over a range of metal concentrations. *J. Colloid Interf. Sci.* **253**, 329–352.

Cross, J.O., Frenkel, A.I., 1999. Use of scattered radiation for absolute X-ray energy calibration. *Rev. Sci. Instrum.* **70**, 38–40.

Diebold, U., 2003. The surface science of titanium dioxide. *Surf. Sci. Rep.* **48**, 53–229.

Dudev, T., Lim, C., 2000. Tetrahedral vs octahedral zinc complexes with ligands of biological interest: a DFT/CDM study. *J. Am. Chem. Soc.* **122**, 11146–11153.

Elzinga, E.J., Reeder, R.J., 2002. X-ray absorption spectroscopy study of Cu²⁺ and Zn²⁺ adsorption complexes at the calcite surface: implications for site-specific metal incorporation preferences during calcite crystal growth. *Geochim. Cosmochim. Acta* **66**, 3943–3954.

Fedkin, M.V., Zhou, X.Y.Y., Kubicki, J.D., Bandura, A.V., Lvov, S.N., Machesky, M.L., Wesolowski, D.J., 2003. High temperature microelectrophoresis studies of the rutile/aqueous solution interface. *Langmuir* **19**, 3797–3804.

Fitts, J.P., Machesky, M.L., Wesolowski, D.J., Shang, X., Kubicki, J.D., Flynn, G.W., Heinz, T.F., Eisenthal, K.B., 2005. Second-harmonic generation and theoretical studies of protonation at the water/α–TiO₂ (110) interface. *Chem. Phys. Lett.* **411**, 399–403.

Fokkink, L.G.J., Dekeizer, A., Lyklema, J., 1987. Specific ion adsorption on oxides—surface-charge adjustment and proton stoichiometry. *J. Colloid Interf. Sci.* **118**, 454–462.

Hiemstra, T., Van Riemsdijk, W.H., 1996. A surface structural approach to ion adsorption: the charge distribution (CD) model. *J. Colloid Interf. Sci.* **179**, 488–508.

Hiemstra, T., Van Riemsdijk, W.H., 2002. On the relationship between surface structure and ion complexation of oxide-solution interfaces. In: Hubbard, A.T. (Ed.), *Encyclopedia of Colloid and Interface Science*. Marcel Dekker, Inc., New York, pp. 3773–3799.

James, R.O., Healy, T.W., 1972. Adsorption of hydrolyzable metal ions at the oxide–water interface. I. Co(II) adsorption on SiO₂ and TiO₂ as model systems. *J. Colloid Interf. Sci.* **40**, 42–52.

Kinniburgh, D.G., 1983. The H⁺/M²⁺ exchange stoichiometry of calcium and zinc adsorption by ferrihydrite. *J. Soil Sci.* **34**, 759–768.

Kinniburgh, D.G., Jackson, M.L., 1982. Concentration and pH dependence of calcium and zinc adsorption by iron hydrous oxide gel. *Soil Sci. Soc. Am. J.* **46**, 56–61.

Kosmulski, M., Maczka, E., 2004. Dilatometric study of the adsorption of heavy-metal cations on goethite. *Langmuir* **20**, 2320–2323.

Kresse, G., Furthmuller, J., 1996. Efficient iterative schemes for ab initio total-energy calculations using a plane-wave basis set. *Phys. Rev. B: Condens. Matter* **54**, 11169–11186.

Lee, S.W., Anderson, P.R., 2005. EXAFS study of Zn sorption mechanisms on hydrous ferric oxide over extended reaction time. *J. Colloid Interf. Sci.* **286**, 82–89.

Lee, Y.J., Elzinga, E.J., Reeder, R.J., 2005. Sorption mechanisms of zinc on hydroxyapatite: systematic uptake studies and EXAFS spectroscopy analysis. *Environ. Sci. Technol.* **39**, 4042–4048.

Lindan, P.J.D., Harrison, N.M., Gillan, M.J., 1998. Mixed dissociative and molecular adsorption of water on the rutile (110) surface. *Phys. Rev. Lett.* **80**, 762–765.

Lowson, R.T., Evans, J.V., 1984. Adsorption and desorption of heavy-metals on alpha-alumina. *Aust. J. Chem.* **37**, 2165–2178.

Machesky, M.L., Wesolowski, D.J., Palmer, D.A., Ichiro-Hayashi, K., 1998. Potentiometric titrations of rutile suspensions to 250 degrees C. *J. Colloid Interf. Sci.* **200**, 298–309.

Machesky, M.L., Wesolowski, D.J., Palmer, D.A., Ridley, M.K., 2001. On the temperature dependence of intrinsic surface protonation equilibrium constants: an extension of the revised MUSIC model. *J. Colloid Interf. Sci.* **239**, 314–327.

Manceau, A., Lanson, B., Drits, V.A., 2002. Structure of heavy metal sorbed birnessite. Part III: Results from powder and polarized extended X-ray absorption fine structure spectroscopy. *Geochim. Cosmochim. Acta* **66**, 2639–2663.

Marcus, Y., 1997. *Ion Properties*. Marcel Dekker, New York.

Miyazaki, A., Matsuo, M., Tsurumi, M., 1996. Surface-complex formation between Zn ions and amorphous aluminosilicate in aquatic systems. *J. Colloid Interf. Sci.* **177**, 335–338.

Monkhorst, H.J., Pack, J.D., 1976. Special points for Brillouin-zone integrations. *Phys. Rev. B* **13**, 5188–5192.

Newville, M., 2001. IFEFFIT: interactive XAFS analysis and FEFF fitting. *J. Synchrotron Radiat.* **8**, 322–324.

Newville, M., Livins, P., Yacoby, Y., Rehr, J.J., Stern, E.A., 1993. Near-edge X-ray-absorption fine structure of Pb: a comparison of theory and experiment. *Phys. Rev. B: Condens. Matter* **47**, 14126–14131.

O'Day, P.A., Chisholm-Brause, C.J., Towle, S.N., Parks, G.A., Brown, J., Gordon, E., 1996. X-ray absorption spectroscopy of Co(II) sorption complexes on quartz (α–SiO$_2$) and rutile (TiO$_2$). *Geochim. Cosmochim. Acta* **60**, 2515–2532.

Okasinski, J.S., Kim, C.-Y., Walko, D.A., Bedzyk, M.J., 2004. X-ray standing wave imaging of the (1/3) monolayer Sn/Ge(111) surface. *Phys. Rev. B: Condens. Matter* **69**, 041401–041404.

Pavlov, M., Siegbahn, P.E.M., Sandström, M., 1998. Hydration of beryllium, magnesium, calcium, and zinc ions using density functional theory. *J. Phys. Chem. A* **102**, 219–228.

Peacock, C.L., Sherman, D.M., 2004. Copper(II) sorption onto goethite, hematite and lepidocrocite: a surface complexation model based on ab initio molecular geometries and EXAFS spectroscopy. *Geochim. Cosmochim. Acta* **68**, 2623–2637.

Perdew, J.P., 1991. Unified theory of exchange and correlation beyond the local density approximation. In: Ziesche, P., Eschrig, H. (Eds.), *Electronic Structure of Solids '91*. Akademic Verlag, Berlin, pp. 110–112.

Peschke, M., Blades, A.T., Kebarle, P., 1999. Formation, acidity and charge reduction of the hydrates of doubly charged ions M^{2+} (Be^{2+}, Mg^{2+}, Ca^{2+}, Zn^{2+}). *Int. J. Mass Spectrom.*, 685–699.

Predota, M., Bandura, A.V., Cummings, P.T., Kubicki, J.D., Wesolowski, D.J., Chialvo, A.A., Machesky, M.L., 2004a. Electric double layer at the rutile (110) surface. 1. Structure of surfaces and interfacial water from molecular dynamics by use of ab initio potentials. *J. Phys. Chem. B* **108**, 12049–12060.

Predota, M., Zhang, Z., Fenter, P., Wesolowski, D.J., Cummings, P.T., 2004b. Electric double layer at the rutile (110) surface. 2. Adsorption of ions from molecular dynamics and X-ray experiments. *J. Phys. Chem. B* **108**, 12061–12072.

Ravel, B., Newville, M., 2005. ATHENA, ARTEMIS, HEPHAESTUS: data analysis for X-ray absorption spectroscopy using IFEFFIT. *J. Synchrotron Radiat.* **12**, 537–541.

Ridley, M.K., Machesky, M.L., Wesolowski, D.J., Palmer, D.A., 2005. Surface complexation of neodymium at the rutile–water interface: a potentiometric and modeling study in NaCl media to 250 degrees C. *Geochim. Cosmochim. Acta* **69**, 63–81.

Rietra, R., Hiemstra, T., Van Riemsdijk, W.H., 1999. The relationship between molecular structure and ion adsorption on variable charge minerals. *Geochim. Cosmochim. Acta* **63**, 3009–3015.

Roberts, D.R., Ford, R.G., Sparks, D.L., 2003. Kinetics and mechanisms of Zn complexation on metal oxides using EXAFS spectroscopy. *J. Colloid Interf. Sci.* **263**, 364–376.

Schindler, P.W., Furst, B., Dick, R., Wolf, P.U., 1976. Ligand properties of surface silanol groups. I. Surface complex formation with Fe^{3+}, Cu^{2+}, Cd^{2+}, and Pb^{2+}. *J. Colloid Interf. Sci.* **55**, 469–475.

Segall, M.D., Lindan, P.J.D., Probert, M.J., Pickard, C.J., Hasnip, P.J., Clark, S.J., Payne, M.C., 2002. First-principles simulation: ideas, illustrations and the CASTEP code. *J. Phys. Condens. Mat.* **14**, 2717–2744.

Shock, E.L., Koretsky, C.M., 1993. Metal-organic complexes in geo-chemical processes: calculation of standard partial molal thermody-namic properties of aqueous acetate complexes at high pressures and temperatures. *Geochim. Cosmochim. Acta* **57**, 4899–4922.

Shvartsburg, A.A., Siu, K.W.M., 2001. Is there a minimum size for aqueous doubly charged metal cations? *J. Am. Chem. Soc.* **123**, 10071–10075.

Spark, K.M., Johnson, B.B., Wells, J.D., 1995. Characterizing heavy-metal adsorption on oxides and oxyhydroxides. *Eur. J. Soil Sci.* **46**, 621–631.

Stern, E.A., 1993. Number of relevant independent points in X-ray-absorption fine-structure spectra. *Phys. Rev. B: Condens. Matter* **48**, 9825–9827.

Stohr, J., Jaeger, R., Brennan, S., 1982. Surface crystallography by means of electron and ion yield SEXAFS. *Surf. Sci.* **117**, 503–524.

Stumm, W., Sigg, L., Sulzberger, B., 1992. *Chemistry of the Solid–Water Interface: Processes at the Mineral–Water and Particle–Water Interface in Natural Systems*. Wiley, New York.

Sverjensky, D.A., 2001. Interpretation and prediction of triple-layer model capacitances and the structure of the oxide-electrolyte-water interface. *Geochim. Cosmochim. Acta* **65**, 3643–3655.

Teschke, O., Ceotto, G., De Souza, E.F., 2000. Interfacial aqueous solutions dielectric constant measurements using atomic force micros-copy. *Chem. Phys. Lett.* **326**, 328–334.

Towle, S.N., Brown, G.E., Parks, G.A., 1999. Sorption of Co(II) on metal oxide surfaces I. Identification of specific binding sites of Co(II) on (110) and (001) surfaces of TiO$_2$ (rutile) by grazing-incidence XAFS spectroscopy. *J. Colloid Interf. Sci.* **217**, 299–311.

Trainor, T.P., Brown, G.E., Parks, G.A., 2000. Adsorption and precip-itation of aqueous Zn(II) on alumina powders. *J. Colloid Interf. Sci.* **231**, 359–372.

Trainor, T.P., Fitts, J.P., Templeton, A.S., Grolimund, D., Brown, G.E., 2001. Grazing-incidence XAFS study of aqueous Zn(II) sorption on α-Al$_2$O$_3$ single crystals. *J. Colloid Interf. Sci.* **244**, 239–244.

Trivedi, P., Axe, L., Tyson, T.A., 2001. An analysis of zinc sorption to amorphous versus crystalline iron oxides using XAS. *J. Colloid Interf. Sci.* **244**, 230–238.

Vanderbilt, D., 1990. Soft self-consistent pseudopotentials in a generalized Eigenvalue formalism. *Phys. Rev. B* **41**, 7892–7895.

Venema, P., Hiemstra, T., Van Riemsduk, W.H., 1996. Comparison of different site binding models for cation sorption: description of pH Dependency, salt dependency, and cation–proton exchange. *J. Colloid Interf. Sci.* **181**, 45–59.

Waychunas, G.A., Fuller, C.C., Davis, J.A., 2002. Surface complexation and precipitate geometry for aqueous Zn(II) sorption on ferrihydrite I: X-ray absorption extended fine structure spectroscopy analysis. *Geochim. Cosmochim. Acta* **66**, 1119–1137.

Wesolowski, D.J., Ziemniak, S.E., Anovitz, L.M., Machesky, M.L., Bénézeth, P., Palmer, D.A., 2004. Solubility and surface adsorption characteristics of metal oxides. In: Palmer, D.A., Fernández-Prini, R., Harvey, A.H. (Eds.), *Aqueous Systems at Elevated Temperatures and Pressures: Physical Chemistry in Water, Steam and Hydrothermal Solutions*. Elsevier Ltd., Amster-dam, pp. 493–595.

Williams, G.D., Soper, A.K., Skipper, N.T., Smalley, M.V., 1998. High-resolution structural study of an electrical double layer by neutron diffraction. *J. Phys. Chem. B* **102**, 8945–8949.

Zabinsky, S.I., Rehr, J.J., Ankudinov, A., Albers, R.C., Eller, M.J., 1995. Multiple-scattering calculations of X-ray-absorption spectra. *Phys. Rev. B* **52**, 2995–3009.

Zhang, C., Lindan, P.J.D., 2003a. Towards a first-principles picture of the oxide-water interface. *J. Chem. Phys.* **119**, 9183–9190.

Zhang, C.J., Lindan, P.J.D., 2003b. Multilayer water adsorption on rutile TiO$_2$ (110): a first-principles study. *J. Chem. Phys.* **118**, 4620–4630.

Zhang, Z., Fenter, P., Cheng, L., Sturchio, N.C., Bedzyk, M.J., Machesky, M.L., Anovitz, L.M., Wesolowski, D.J., 2006. Zn^{2+} and Sr^{2+} adsorption at the TiO$_2$ (110)-electrolyte interface: influence of ionic strength, coverage, and anions. *J. Colloid Interf. Sci.* **295**, 50–64.

Zhang, Z., Fenter, P., Cheng, L., Sturchio, N.C., Bedzyk, M.J., Mache-sky, M.L., Wesolowski, D.J., 2004a. Model-independent X-ray imag-ing of adsorbed cations at the crystal-water interface. *Surf. Sci.* **554**, L95–L100.

Zhang, Z., Fenter, P., Cheng, L., Sturchio, N.C., Bedzyk, M.J., Predota, M., Bandura, A., Kubicki, J.D., Lvov, S.N., Cummings, P.T., Chialvo, A.A., Ridley, M.K., Benezeth, P., Anovitz, L., Palmer, D.A., Machesky, M.L., Wesolowski, D.J., 2004b. Ion adsorption at the rutile–water interface: linking molecular and macroscopic properties. *Langmuir* **20**, 4954–4969.